Journal of Medicinal Chemistry

Article

A new fluorogenic small molecule labeling tool for surface diffusion analysis and advanced fluorescence imaging of #-site amyloid precursor protein (APP)-cleaving enzyme 1 based on silicone rhodamine: SiR-BACE1

Sandra Karch, Johannes Broichhagen, Julia Schneider, Daniel Böning, Stephanie Hartmann, Benjamin Schmid, Philipp Tripal, Ralf Palmisano, Christian Alzheimer, Kai Johnsson, and Tobias Huth

J. Med. Chem., **Just Accepted Manuscript** • DOI: 10.1021/acs.jmedchem.8b00387 • Publication Date (Web): 25 Jun 2018

ACS Publications

is published by the American Chemical Society. 1155 Sixteenth Street N.W., Washington, DC 20036

A new fluorogenic small molecule labeling tool for surface diffusion analysis and advanced fluorescence imaging of β-site amyloid precursor protein (APP)-cleaving enzyme 1 based on silicone rhodamine: SiR-BACE1

Sandra Karch [§,1], Johannes Broichhagen [§,2,3], Julia Schneider [§,1], Daniel Böning [4], Stephanie Hartmann [1], Benjamin Schmid [5], Philipp Tripal [5], Ralf Palmisano [5], Christian Alzheimer [1], Kai Johnsson [§§,2,3], Tobias Huth* [§§,1]

[1] Institute of Physiology and Pathophysiology, Friedrich-Alexander-Universität Erlangen-Nürnberg, Universitaetsstraße 17, 91054 Erlangen, Germany.

[2] Department of Chemical Biology, Max Planck Institute for Medical Research, Jahnstraße 29, 69120 Heidelberg, Germany.

[3] Laboratory of Protein Engineering, Institut des sciences et ingénierie chimiques, Sciences de base, École Polytechnique Fédérale Lausanne, 1015 Lausanne, Switzerland.

[4] Max Planck Institute for the Science of Light, Staudtstraße 2, 91058 Erlangen, Germany.

[5] Optical Imaging Centre, Friedrich-Alexander-Universität Erlangen-Nürnberg, Hartmannstraße 14, 91052 Erlangen, Germany.

Abstract

β-site APP-cleaving enzyme 1 (BACE1) is a major player in the pathogenesis of Alzheimer's disease. Structural and functional fluorescence microscopy offers a powerful approach to learn about the physiology and pathophysiology of this protease. Up to now, however, common labeling techniques either require genetic manipulation, use large antibodies, or are not compatible with live cell imaging. Fluorescent small molecules that specifically bind to the protein of interest can overcome these limitations. Herein, we introduce **SiR-BACE1**, a conjugate of the BACE1 inhibitor S-39 and SiR647, as a novel fluorogenic, tag-free, and antibody-free label for BACE1. We present its chemical development, characterize its photo-physical and pharmacologic properties, and evaluate its behavior in solution, in over-expression systems, and in native brain tissue. We demonstrate its applicability in confocal, stimulated emission depletion (STED), and dynamic single molecule microscopy. First functional studies with **SiR-BACE1** on the surface mobility of BACE1 revealed a markedly confined diffusion pattern.

Introduction

First described by Alois Alzheimer over a century ago, Alzheimer's disease (AD) is the most common form of dementia with progressive cognitive impairment including memory and speech deficits, spatial disorientation, apraxia, and psychiatric symptoms.[1] Most cases can be classified as sporadic AD, for which age is a major risk factor.[2,3] Due to the aging population, AD is expected to become a growing socio-economic challenge in the upcoming decades.[4]

The brains of AD patients display two histopathological characteristics: i) amyloid plaques, which mainly consist of accumulated Aβ peptides, and ii) neurofibrillary tangles formed by aggregated hyper-phosphorylated tau protein.[5] Despite a still incompletely understood etiology, vast evidence supports the amyloid cascade hypothesis, which suggests a deregulated Aβ homeostasis as an early step in the pathogenesis.[6–9] Aβ is generated by two-step proteolysis from amyloid precursor protein (APP). The first and rate-limiting step is catalyzed by β-site APP-cleaving enzyme 1 (BACE1).[10–14] BACE1 is an aspartic protease, mainly located in the trans-Golgi network and the endosomal pathway, which undergoes pronounced surface trafficking and recycling to early endosomes, where it co-localizes with and processes APP.[15–17] Predisposing or protecting hereditary APP mutations that affect processing rates at the β-site underscore the pathogenic impact of BACE1.[18–21]

Current knowledge on physiological and pathological, proteolytic and non-proteolytic functions of BACE1 is based on decades of research including animal, histological, biochemical, electrophysiological, and optical studies. [5,17,22,23] Light microscopy has contributed to some of the key findings: Immunofluorescence demonstrated that BACE1 is expressed in mossy fiber synapses of the hippocampal formation, which belongs to the brain regions that are affected by the earliest pathologic changes and are central for memory formation and retrieval.[24,25] Antibody staining also showed that BACE1 accumulates near amyloid plaques in dystrophic neurites, being associated with impaired lysosomal degradation

and possibly fostering Aβ secretion.[26,27] BACE1 and APP surface trafficking is independent from each other, as illustrated by total internal reflection fluorescence (TIRF) microscopy using fusions of the proteins to pH-sensitive fluorescent indicators.[28] Fluorescence resonance energy transfer (FRET) between antibodies directed against tagged proteins revealed close encounter between BACE1 and APP in early endosomes.[15] A fluorescence complementation approach with BACE1 and APP fusion proteins recently visualized their interaction in neurite microdomains and axonal BACE1-APP co-trafficking, translating previous work to the neuronal environment.[29]

Interrogation of BACE1 in over-expression systems and in non-neuronal cell lines may not necessarily give a full and unbiased account of its many actions in the healthy and diseased brain. This holds in particular for all approaches using fluorescence imaging, where bulky labels impose steric hindrances, thereby possibly affecting BACE1 trafficking and regulation. Given the constraints of conventional imaging tools, alternative specific, bright, and easy-to-apply labeling solutions are eagerly awaited to visualize BACE1 molecules and track their subcellular pathways and interaction sites at the highest spatiotemporal resolution.

Because of the central role of BACE1 in AD pathogenesis, great efforts were made to develop small molecule BACE1 inhibitors.[30,31] Despite some setbacks, inhibition of BACE1, most promising as part of a multitarget combination therapy, has remained a rational strategy to prevent and treat AD.[32–35] Aminohydantoins have been introduced as a class of inhibitors that contact the catalytic aspartates, inhibit BACE1 at sub-micromolar concentrations, and possess good brain permeability.[36] The derivative S-39 exhibits a low nanomolar inhibitory potency and shows excellent selectivity over related proteases in screenings *in vitro*.[37,38]

To meet the urgent needs for innovative BACE1 visualization strategies, we made use of the pre-clinical inhibitor S-39 as a starting point to build a novel BACE1 labeling tool. Here, we introduce an organic conjugate that exploits the high affinity and specificity of S-39 in

combination with the far-red silicon-rhodamine derivative SiR647 and demonstrate the viability and functionality of this new approach.

Results

A novel fluorogenic probe for BACE1 visualization

We aimed to develop a probe for BACE1 labeling independent of tags and with a good signal-to-noise ratio based on fluorogenicity (Figure 1A).[39] Therefore, we started to design conjugates of the fluorogenic silicone-rhodamine derivative SiR647 (Figure 1B). The small molecule BACE1 inhibitor S-39 [37] was linked to the dye *via* methylene linkers of different lengths that drag the conjugate into the active site pocket of BACE1. Binding to the protein should bring the SiR647 component into the polar environment of the protein surface and cause a conformational switch from its non-fluorescent spirolactone form to its fluorescent zwitter-ion, as shown in Figure 1B. The linkers ranged from 2 to 8 methylene spacers (conjugates C2 to C8) and were synthetically introduced late-stage, a fact that allows flexible alteration, optimization and synthetic economy (Figure 1C). In order to do so, a multistep synthetic sequence was performed, starting from acetonedicarboxylic acid (**1**) and propionic anhydride (**2**) to obtain bromo pyridine **3** according to a previously reported procedure from Li *et al*.[40] Silicon rhodamine (SiR) **4** was functionalized after activation with TSTU and coupling to diamines with several linker lengths (denoted by n), before a guanidine was installed on the primary amine to obtain **5a-f** (see Supplementary Tables 1 and 2). In parallel, the main pharmacophore was built from commercially available boronic acid **6** and 3-bromoiodobenzene (**7**) by a iodo-selective Suzuki reaction that gave access to bromo aryl **8**. Next steps were a Sonogashira reaction with trimethylsilyl acetylene (to obtain **9**), deprotection (to obtain **10**) and subsequent Sonogashira reaction with previously obtained **3** to obtain internal alkyne **11**. Triple bond oxidation of **11** with permanganate yielded 1,2-bisketone **12**, that underwent benzilic rearrangement with SiR-linked guanidines. This straightforward access to SiR-linked probes **13a-f** gave access to several possible fluorogenic BACE1 inhibitors (see Supplementary Table 3).

We next investigated the photo-physical properties of our conjugates in solution. Figure 1D and E show the excitation and emission spectra for the C4 conjugate, termed **SiR-BACE1**. Absorption was maximal at 651 nm and emission was observed at around 660-680 nm with its maximum at 674 nm (Figure 1D). To control whether SiR647 had preserved its fluorogenicity as a component of the conjugate, we recorded the absorption in PBS with or without the addition of 0.2% SDS (Figure 1E). In the absence of detergent, the probe lost its ability to absorb light in the range of 650 nm, hence our conjugates were fluorogenic. In this experiment, fluorogenicity was promoted by the non-polar environment of SDS micelles.[39] To determine whether the fluorogenic on-switch is also mediated by specific binding to BACE1, we recorded **SiR-BACE1** emission in the absence or presence of recombinant BACE1 protein (Figure 1F). The target protein increased fluorescence in the expected spectral range, which confirmed BACE1-mediated fluorogenic on-switch.

BACE1 binding, inhibition, and visualization by a C4-linker S-39/SiR647 conjugate

Effective BACE1 labeling by the compound happens in two steps: binding of the probe and switching to its fluorescent form. Thus, we aimed to identify conditions that promote both. In a first experiment, we over-expressed hBACE1-EGFP in HEK293T cells and stained with all conjugates of different linker length. hBACE1-EGFP located mainly to the plasma membrane and intracellular compartments near the nucleus (Figure 2A, middle panel). At medium linker lengths (C4 to C6), our conjugates showed the strongest co-staining (Figure 2A, bottom panel), indicating efficient binding to BACE1 and switching to the on-state, with C4 displaying the highest intensities.

From the data in Figure 2A, we generated color-coded 2D histograms of EGFP and SiR647 intensities to further evaluate the co-staining (Figure 2B). For all linker lengths, we observed

two areas of co-localized pixels in the whole frame co-localization plots, which could be assigned to pixels at the plasma membrane (membrane ROI, middle panel) or pixels of perinuclear clusters (cluster ROI, bottom panel). At the plasma membrane, the C4 and C5 conjugates showed the most intense staining, indicated by the steepest correlation and numerous pixels with high SiR647 intensities (Figure 2B, middle panel). In perinuclear cluster regions, C4 was clearly superior to the other substances, giving the highest SiR647 signals (Figure 2B, bottom panel). Given these results, we chose C4 as our BACE1 labeling probe, which we termed **SiR-BACE1**.

Next, we reasoned that binding of the conjugate to the active site pocket of BACE1 should inhibit its proteolytic activity, like the parent drug S-39. To determine and quantify inhibition of BACE1 by increasing concentrations of the different conjugates, we performed a FRET-based enzymatic assay (Figure 2C) using a synthetic BACE1 substrate coupled to a donor fluorophore, which is quenched until substrate cleavage by BACE1. All conjugates indeed inhibited BACE1 in a dose-dependent manner, with BACE1 being more efficiently suppressed by conjugates with longer linkers (Figure 2D). Plotting the IC_{50} values of all linker lengths and performing a cluster analysis, the IC_{50} of conjugates with 2 or 3 methylene spacers (C2, C3) clustered around 1700 nM, while IC_{50} of conjugates with 4 or more methylene spacer groups (C4-C6, C8) clustered around 1100 nM. We conclude that conjugates were slightly hindered in binding by a linker length $\leq$3 carbon atoms but perform equally well above that threshold. Staining differences as observed in Figure 2A must hence be due to varying fluorogenic conversion.

Acidic conditions promote fluorogenicity of SiR-BACE1

Both binding of small molecule inhibitors to the active site pocket of BACE1 [41] and SiR647 protonation for the fluorescent on-switch are pH-dependent, preferring acidic conditions. Consequently, we evaluated the effect of acidic pH on **SiR-BACE1** binding to BACE1 and its

fluorogenicity. In order to have an experimental setup with controlled environment, we chose a cell-free approach using fluorescence correlation spectroscopy (FCS) as a read-out, analyzing **SiR-BACE1** diffusion and its brightness. First, we characterized free **SiR-BACE1** diffusion in HBS pH 5 in the absence of BACE1 (Figure 3A). The auto-correlation curves from 3 independent experiments over 30x 10 s were fitted to a 1-component 3D translational model, determining the diffusion time, triplet fraction and relaxation time, number of molecules, and the structural parameter of the point spread function. The structural parameter was freely fitted in all FCS experiments and typically ranged from 5 to 7. The diffusion time of 100 nM **SiR-BACE1** was 72 ± 3 µs (mean ± SE), serving as a reference in following experiments. We next explored how **SiR-BACE1** diffusion changes upon adding recombinant BACE1 extracellular domain (ECD). On-stage, 2 µM BACE1 ECD were added to **SiR-BACE1**, instantly followed by time-lapse FCS recording over 500x 10 s. The auto-correlation curves of each 10 s-interval were fitted to a 2-component 3D translational model with one diffusion time being fixed to 72 µs for freely diffusing **SiR-BACE1** (see above). The diffusion time of the second fraction was determined by the fit and was always higher than the fixed first fraction, indicating a slowly diffusing second population. The fraction of **SiR-BACE1** that belonged to this slow fraction increased over time (Figure 3B) with a $t_{0.5}$ of 13 ± 1 min (mean ± SE). This prompted us to incubate **SiR-BACE1** with BACE1 ECD for 30 min before performing end-point FCS recordings in the following set of experiments to allow **SiR-BACE1** to bind and convert into the fluorescent zwitter-ionic conformation. The diffusion time of the slow fraction in Figure 3B equaled 549 ± 3 µs (mean ± SE, N = 3 recordings) and did not change systematically over time (Figure 3C), serving as a reference for diffusion of BACE1-bound **SiR-BACE1**.

To evaluate the effect of pH, end-point FCS was recorded over 30x 10 s from **SiR-BACE1** in the presence of different concentrations of BACE1 ECD in pH 5 or 7.4. Upon binding to BACE1 ECD, we expected **SiR-BACE1** diffusion to decelerate (indicated by longer diffusion

times, see Figure 3D) and **SiR-BACE1** fluorescence to increase (indicated by rising count rates). Auto-correlation curves (Figure 3D) were parameterized by fitting to the 2-component 3D translational model with the diffusion times being fixed to 72 and 550 µs (see above). With increasing concentrations of BACE1 ECD, a growing **SiR-BACE1** fraction diffused slowly, i.e. BACE1-dependent (Figure 3D), and the fluorescence signal became more intense. We first compared the influence of pH on the fraction of slowly-diffusing **SiR-BACE1** (Figure 3E). At pH 5, the half-maximal effect was reached at 27 ± 4 nM BACE1 ECD (mean ± SEM), while at pH 7.4, the apparent EC_{50} was 87 ± 33 nM. Note that the analysis is biased towards the slowly diffusing BACE1-bound fluorophores because of the fluorogenic on-switch. When we focused on photon counts, acidic pH enabled bright fluorescence at lower BACE1 ECD concentrations than slightly alkaline pH (Figure 3F), with EC_{50} values of 45 ± 6 nM and 620 ± 130 nM at pH 5 and 7.4, respectively. These results showed that acidic pH likely supports both binding and fluorogenicity. While the effect on binding was not pronounced enough to be statistically significant, acidic conditions clearly support the fluorescent on-switch.

We next evaluated whether a positive effect of acidic pH holds true for staining of BACE1-EGFP in HEK293T cells. In a first experiment, we stained living cells with **SiR-BACE1** in pH 5 or pH 7.4 (Figure 3G). The intracellular compartments, presumably trans-Golgi network (pH ~6), were stained brightly in both conditions. The plasma membrane, however, where BACE1 molecules are exposed to our staining buffer's pH, was labelled by **SiR-BACE1** at pH 5, but not at pH 7.4. To determine whether lacking membrane staining was due to the absence of binding or to a non-fluorescent conformation of the fluorophore, we performed a two-step experiment with fixed HEK293T cells over-expressing hBACE1-EGFP. Cells were stained with **SiR-BACE1** in pH 7.4, washed, and observed in time-lapse imaging for 60 min in pH 7.4 before the imaging buffer's pH was adjusted to pH 5, followed by another 60-min observation (Figure 3H). The change of buffer pH was followed by a decrease of the EGFP

fluorescence signal, while in the **SiR-BACE1** channel, fluorescence increased and plasma membranes of the transfected cells became visible. This observation indicates that **SiR-BACE1** can be bound at pH 7.4 in its fluorescent off-state, and can switch to its fluorescent conformation upon pH change.

To further discriminate between pH-dependent binding and pH-dependent fluorescent switching, we performed an additional cell-free experiment. Binding of **SiR-BACE1** to BACE1 was examined with the FRET-based BACE1 activity assay (see Figure 2C), performed in HBS of pH 5, 7.4, or 8 instead of the supplied assay buffer. Processing of the BACE1 substrate was controlled by a kinetic assay run, as suggested by the manufacturer. In an endpoint assay, activity of BACE1, indicated by the intensity of unquenched cleavage product, was significantly lower in pH 7.4 and 8 when compared to pH 5, as expected (Figure 3I, upper panel).[42,43] For all three conditions, we determined the IC_{50} for BACE1 inhibition by **SiR-BACE1** as illustrated in Figure 2C and found that inhibition was not significantly changed by pH (Figure 3I, lower panel).

Cellular affinity and specificity

Applying acidic conditions for staining, we quantified the affinity of **SiR-BACE1** for BACE1 in a cellular environment. HEK293T cells over-expressing hBACE1-EGFP were stained with different concentrations of **SiR-BACE1**, ranging from 1 to 5000 nM, in pH 5. Flow cytometry allowed us to correlate intensities of hBACE1-EGFP and SiR647 signals from individual cells (Figure 4A). The slope of the correlation curve indicates how efficiently **SiR-BACE1** has stained the hBACE1-EGFP molecules. Figure 4A depicts the distribution of cells, which were stained with 1 (grey dots), 100 (green dots), or 1000 nM **SiR-BACE1** (red dots). At low EGFP channel intensities (i.e. in non-transfected cells), no correlation with **SiR-BACE1** signal was observed. For higher hBACE1-EGFP intensities (i.e. transfected cells), the **SiR-BACE1** signal positively correlated with the expression level of hBACE1-EGFP. A bilinear

custom fit with a constant first and ascending proportional second part appeared suitable to parameterize this distribution. A small fraction of cells with a very high intensity in the EGFP channel deviated from the correlation towards higher **SiR-BACE1** signals. Since we had observed that such "hyper-expressing cells" lose their membrane integrity, this population was not considered.

Increasing **SiR-BACE1** concentration lead to a systematic change of the cells' fluorescence distribution, represented by the bilinear fit (Figure 4A): The level of the first component stays low for staining with 100 nM, but rises for staining with 1000 nM of **SiR-BACE1**. We interpreted an increased level as an unspecific accumulation of **SiR-BACE1** in all cells, irrespective of the presence of hBACE1-EGFP. The slope of the second, proportional component of the fit increased with increasing **SiR-BACE1** concentrations (cf. 1 to 100 nM), indicating enhanced probability for a hBACE1-EGFP molecule to be stained by **SiR-BACE1**. Upon further increase of **SiR-BACE1** concentration (cf. 100 to 1000 nM), the slope hardly increased further, indicating saturation of hBACE1-EGFP. The proportionality factor was plotted as a function of **SiR-BACE1** concentration to illustrate specific staining (Figure 4B). The EC_{50} of **SiR-BACE1** for BACE1 staining was determined to be 78 ± 18 nM. In this concentration range of **SiR-BACE1** (see green dataset in Figure 4A), the constant part of the fit did not indicate relevant unspecific accumulation of **SiR-BACE1** in non-transfected cells, demonstrating that specific staining is feasible in HEK293T cells.

In this experimental system, specific BACE1 staining could be unambiguously confirmed by a competition experiment against the benchmark small molecule BACE1 inhibitor IV (Merck), also known as C3 ($IC_{50} = 15$ nM).[44] HEK293T cells expressing hBACE1-EGFP were stained with 70 nM **SiR-BACE1** in the presence of different concentrations of inhibitor IV. Increasing concentrations of inhibitor IV displaced **SiR-BACE1** (Figure 4C) with an IC_{50} of 55 ± 8 nM, which was determined by a fit according to Equation 1. The successful

competition between the two substances argues in favor of the same orthosteric binding site for inhibitor IV and **SiR-BACE1**.

In addition, we performed control experiments to confirm that **SiR-BACE1** specifically binds to the BACE1 active site in HEK293T cells (Figure 4D). The proteins of interest were over-expressed as fusion proteins with EGFP. We stained cells over-expressing the proteolytically inactive mutant D289N of BACE1, which was expected not to bind **SiR-BACE1** due to the mutated catalytic site. Additionally, we tested whether **SiR-BACE1** stains the BACE1 homolog BACE2 or the BACE1-related aspartyl protease cathepsin-D. Indeed, none of these three proteins evoked significant staining by **SiR-BACE1**.

SiR-BACE1 is STEDable

With this new tool in our hands, we explored several feasible applications that may profit from **SiR-BACE1**'s unique feature of being a fluorogenic, specific, and tag-independent label for BACE1. As first application, we used **SiR-BACE1** for super-resolution imaging of over-expressed BACE1 in the neuronal cell line N1E-115. The probe reproduced the pattern of BACE1 indicated by its EGFP tag (Figure 5A-B). We scanned neurite details in confocal and stimulated emission depletion (STED) mode (Figure 5C). BACE1, visualized by **SiR-BACE1**, was present in the soma and in neurites. Unlike the confocal recording, the STED image resolved the vesicular distribution of the protein. For comparison, we plotted representative profiles from a confocal *versus* a STED image for a cross profile (Figure 5C, green box and graph) and neighboring vesicular structures (red box and graph), which demonstrate the gain in resolution by using **SiR-BACE1** for STED microscopy.

Visualization of endogenous BACE1

Having applied **SiR-BACE1** successfully on samples over-expressing EGFP-tagged BACE1, we next used it to visualize endogenous BACE1. As a sample, we chose native hippocampal brain slices from wild-type and BACE1 knockout (KO) mice. **SiR-BACE1** stained the hilus of the dentate gyrus and the mossy fiber terminals in the CA3 region (Figure 6A and B, left panels), consistent with the BACE1 expression pattern described before.[24,45,46] In slices from knockout animals, no equivalent BACE1 staining was observed (Figure 6A, right panel), confirming specificity of **SiR-BACE1** for in-situ-detection of endogenous BACE1. To further support the finding that **SiR-BACE1** does indeed specifically detect BACE1, we performed a competition experiment with BACE1 inhibitor IV (see above). At 20-fold excess, inhibitor IV displaced most of the **SiR-BACE1** from the active site and suppressed BACE1 staining (Figure 6B, right panel).

We also tested **SiR-BACE1** for staining of living hippocampal neuronal cultures, in which the probe provoked intense staining of somatic and neuritic structures, both in wild-type and knockout preparations (Figure 6C). To elucidate the origin of these accumulations, we co-stained mouse embryonic fibroblasts (MEF) from BACE1 knockout mice with **SiR-BACE1** and LysoTracker. Co-localization implied **SiR-BACE1** accumulations in acidic lysosomes (Figure 6D, upper panel). We asked whether **SiR-BACE1** accumulated because of an off-target present in lysosomes or due to the acidic pH of the compartment. With bafilomycin A1 (BafA1), we disrupted lysosomal acidification. Disappearance of the LysoTracker signal confirmed neutralization. With BafA1 treatment, lysosomal **SiR-BACE1** staining was abolished (Figure 6D, lower panel), arguing for a pH-dependent accumulation. A pre-treatment of the primary neuronal cultures with BafA1 to establish a specific staining was not considered because control experiments with BafA1 in MEF cells had shown that BACE1-EGFP, as well as additional transmembrane and membrane-associated proteins, lost its typical expression pattern. We concluded that **SiR-BACE1** is not suited for staining of primary

hippocampal neurons under the tested circumstances, but well applicable for BACE1 detection in frozen sections, which do no longer contain acidified vesicles (Figure 6A,B).

Single particles tracking reveals confined membrane diffusion of BACE1

Finally, we wanted to investigate the behavior of single BACE1 molecules at the cell surface. The diffusion and trafficking dynamics of BACE1 have been recently implicated in the pathogenesis of Alzheimer´s disease.[5,47,48] Therefore, BACE1 surface movement is getting increasing attention, but dynamic data are not available yet. The development of **SiR-BACE1** offers now the unprecedented opportunity to track single BACE1 molecules without the hindrance of tags or huge antibody labels.

The experiments with neuronal cultures and MEF cells (Figure 6) taught us that accumulations of **SiR-BACE1** in acidic intracellular compartments may impair BACE1 visualization when it comes to detection of low endogenous levels – or single molecules. We therefore worked with plasma membrane lawns (PML) of CHO-K1 cells,[49] with intracellular organelles being removed to achieve the best possible signal-to-background ratio.

Wild-type human BACE1 was transiently expressed at low levels and stained with **SiR-BACE1**, resulting in spot-like, diffraction-limited signals of single BACE1 molecules (Figure 7A, right panel). Unstained transfected PML and non-transfected stained PML did not show relevant autofluorescence or unspecific staining, respectively (Figure 7A, left and middle panel). Tracks of BACE1 diffusion (Figure 7B) were generated from time-lapse recordings of 6 PML regions from 4 cells. Track fluorescence intensity was averaged over time and plotted for all tracks (Figure 7C). Intensities followed a bi-modal Gaussian distribution. 50% of the tracks showed a relative intensity of 6.6 ± 2.4 AU (mean ± SE). The intensity of the remaining tracks was 12 ± 5 AU. The velocity of the molecules did not correlate with their intensity (Figure 7D). Tracks were typically shorter than 1-2 s (Figure 7E). Mobility of the tracked molecules was independent from track lifetime (Figure 7F). Therefore, the track

population was assumed to be homogenous regarding diffusion behavior. Plotting the mean square displacement (MSD) over time revealed a confined diffusion of the BACE1 molecules, indicated by the negative deviation of the data from a linear diagonal (Figure 7G, black dots). As described previously,[50] the mobility distribution (Figure 7H) did not fit to a γ-distribution, thereby excluding free diffusion. 15% of the tracks, i.e. 220 tracks, were immobile (defined by a mobility < 0.02 $\mu m^2/s$)[50]. When we excluded these from the analysis, the mobile BACE1 fraction still showed restricted movement (Figure 7G, green dots).

To validate that the observed traces originated from single **SiR-BACE1** molecules, PMLs were fixed to immobilize the proteins and then stained with **SiR-BACE1**. The presence of a PML was confirmed by an area showing smooth fluorescence of membrane-targeted EGFP (Figure 7I). Expression of SNAP-tagged hBACE1 was confirmed by staining with the SNAP substrate SNAP-surface549. **SiR-BACE1** staining resulted in distinct BACE1 signals comparable to the **SiR-BACE1** pattern in live PML (Figure 7I, cf. A, right panel). The signals had been efficiently immobilized by the fixation (cf. 0 s vs. 10 s in Figure 7J) and typically disappeared from one frame to the other in one-step bleaching, confirming the presence of single fluorophores (Figure 7J, arrows).

Discussion and Conclusions

The aim of this study was to design and evaluate a small molecule BACE1 labeling tool that fulfils the following criteria: It marks the protease for fluorescence imaging without genetic manipulation or antibodies, it is easy to apply, and it is compatible with a broad range of imaging systems. We succeeded in developing the fluorogenic probe **SiR-BACE1** as a conjugate of the small molecule BACE1 inhibitor S-39 for selective targeting and the far-red dye SiR647 (Figure 1). Following a one-step staining procedure, **SiR-BACE1** can visualize recombinant BACE1 in solution (Figure 2C-D, Figure 3A-F), over-expressed BACE1 (Figure 2A-B, Figure 3G-H, Figure 4, Figure 5, Figure 7), and endogenous BACE1 (Figure 6). **SiR-BACE1** staining rendered BACE1 accessible for confocal laser scanning microscopy (Figure 2A, Figure 6), super-resolution imaging by Stimulated Emission Depletion (STED, Figure 5), and single molecule time-lapse analysis (Figure 7).

Choice of a linker

A key aspect in the synthetic strategy was the late-stage coupling of the pharmacophore to the fluorophore, which allows easy modulation of the derivatives' linker. We selected a linker length of 4 methylene spacers (C4), which proved to be critical for sensitive labeling. Conjugates with shorter linker had a slightly lower affinity for the BACE1 active site (Figure 2D). Longer linkers, like in the C8 compound, did allow undisturbed binding to and inhibition of BACE1, but resulted in low fluorescence, which likely was a consequence of insufficient fluorescent conversion of bound conjugate from its non-fluorescent spirolactone form to the fluorescent zwitter-ion. Overall, the C4 compound, which we termed **SiR-BACE1**, allowed binding of the inhibitor with low steric hindrance by SiR647 and brought the fluorophore close enough to the protein surface to promote its fluorogenic on-switch.

pH dependency

In the endosomal pathway, pH decreases from a slightly alkaline extracellular pH to pH 5-6.[51] Based on the chemistry of SiR647,[39] the acidic pH should support labeling by enforcing the fluorescent on-switch of the dye. Indeed, that effect was clearly observed for BACE1 in solution (Figure 3F) as well as for over-expressed BACE1 in cells (Figure 3H).

In addition, BACE1 active site residues have been shown to change their hydration state depending on pH, which results in the enzymatic pH optimum of 4.5.[42,43] Like substrate cleavage, binding of small molecule inhibitors into the active site pocket has been shown to depend on the charges of the respective side chains.[41,52] Previous work has pointed out that the pH profile of small molecule binding to BACE1 is dependent on how the small molecule interacts with BACE1.[53] We checked for pH dependency by cell-free FCS and found a tendency for enhanced binding at pH 5 (Figure 3E). Superior staining of over-expressed BACE1 in pH 5, as demonstrated in Figure 3G, is mainly attributable to a promoted fluorogenic on-switch.

Acidic accumulation

Inhibitory potency of **SiR-BACE1** was 100-fold lower than that of the parent drug S-39 in a cell-free enzymatic assay (IC_{50} S-39: 10 nM).[37] Only a factor 2 can be attributed to the fact that **SiR-BACE1** was obtained as a racemate. We conclude that the conjugation of the drug to SiR647 diminishes its potency of binding to the BACE1 active site pocket, an effect that has been observed before.[54] Arguing for steric hindrance is supported by the finding that short linker lengths, which bring SiR647 close to the pharmacophore, slightly decrease BACE1 inhibition.

When compared to the inhibitory potency in the cell-free FRET assay, the effective concentration for staining BACE1 in the cellular environment was 14-fold lower with an EC_{50}

of 78 ± 18 nM. Such an observation is not unprecedented: A study that evaluated a small molecule labeling tool for cathepsin-D, another aspartyl protease, revealed a similar effect.[55] The compound in that study accumulated in acidic compartments and thereby reached an increased affinity for cathepsin-D in cells versus in-vitro-assays by one to two orders of magnitude. Considering such a mechanism for **SiR-BACE1**, it is important to note that SiR647 changes its conformation in acidic pH.[39] Acidic trapping of **SiR-BACE1** therefore seemed possible. Support for this hypothesis came from the staining of primary hippocampal neurons by **SiR-BACE1**: When we analyzed those for endogenous BACE1 staining, prominent unspecific **SiR-BACE1** accumulations occurred in an irregular pattern and impeded BACE1 visualization in this sample (Figure 6C). Further characterization in BACE1 knockout MEF cells confirmed that **SiR-BACE1** is entrapped into acidic lysosomes. This local accumulation can fully explain the higher apparent affinity of **SiR-BACE1** in the cellular system when compared to the cell-free FRET assay.

Given the high-affinity EC_{50} in cellular staining, it may seem surprising that only a minor fraction of BACE1 in plasma membrane lawns (PMLs) was stained by 100 nM **SiR-BACE1** (Figure 7I). However, the staining situation rather resembles the cell-free assay than the cellular staining with locally increased **SiR-BACE1** concentrations. In the homogenous staining solution above PMLs, **SiR-BACE1** does not accumulate and may therefore not be able to saturate all present BACE1 molecules in the preparation. An alternative explanation for non-saturated staining in PMLs could be that **SiR-BACE1** may prefer binding to a certain multimeric form of BACE1 that may occur predominantly intracellularly. However, that seems unlikely since recent work has identified BACE1 multimers in an equal distribution between subcellular compartments.[56]

SiR-BACE1 for confocal imaging and nanoscopy

When a protein of interest is labelled using primary and dye-coupled secondary antibodies, one target molecule is estimated to be stained by approximately 25 fluorophores yielding a bright signal. In super-resolution imaging, however, this apparent advantage due to "antibody piling" has the adverse effect of separating the fluorophores by approximately 20 nm from the target protein. Such spacing is unacceptable for techniques that offer spatial resolution in the nanometer[57] or even Angstrom scale, like the novel extension of STORM imaging at cryo temperatures (Cryogenic Optical Localization in 3D, COLD)[58]. A super-resolution label hence is a trade-off between photon yield and label size. In addition, ratiometric analysis and sub-nanometer structural investigations require a 1-to-1 labeling. **SiR-BACE1** meets these diverging criteria by i) depositing one fluorophore per BACE1 molecule, ii) dragging the dye into the active site pocket, resulting in the minimal possible distance between BACE1 and the label, and iii) containing SiR647, which offers a high photon yield and excellent photo-stability[39]. The latter compensates partially for the low number of deposited fluorophores. Owing to these features, **SiR-BACE1** allowed STED imaging, which required long exposure times because of low expression level and fluorophore concentration. In addition, visualization of endogenous BACE1 in native hippocampal slices, where fluorophore concentration is naturally limited, (Figure 6A,B) similarly profited from **SiR-BACE1**'s features. Both measurements would have been impossible with a low-yield or fast-bleaching fluorophore. Judging from these applications, we can advocate **SiR-BACE1** for super-resolution, low-light, and single molecule applications.

Single molecule BACE1 diffusion analysis

Label size is not just a factor when discussing the distance to the target protein, but also matters because of its sheer mass and diameter: Analysis of single molecules in the plasma

membrane has mostly been done with fluorescent protein fusion constructs,[50,59,60] antibodies labelled with quantum dots,[61] or self-labeling enzymes like the SNAP tag.[62,63] Since these labels can reach the same size as the analytes or even exceed their dimensions, they may confound optical recordings in several aspects. For instance, SNAP tag has been shown to slow the movement of a protein of interest[63] and antibodies are commonly used to even immobilize proteins at the cell surface[64]. Additionally, tags interfere with protein-protein interactions. Incorporation of fluorescent unnatural amino acids has minimized tag size but requires genetic manipulation of the target protein.[65] Interferometric detection of scattering (iSCAT) allows observation of molecules without any label but is not yet available to the broad life science community and is currently limited to the detection of secreted proteins.[66,67] Thus, single molecule tracking of membrane proteins still requires a label, which should be as small as possible, such as fluorophore conjugates of receptor agonists or antagonists.[63,65,68] These small molecules are fabricated against specific targets and, with **SiR-BACE1**, we introduce the first such label for BACE1.

Employing this imaging tool, we are now able to probe the motility of BACE1 in cellular membranes. Our data argue for a confined diffusion behavior of the secretase, which was not dependent on diffusion coefficient, track length, or intensity. This finding strongly suggests that BACE1 molecules form a homogenous population in the plasma membrane that does not diffuse freely. We are aware that our characterization of BACE1 diffusion may be cell type-specific, as reported for other transmembrane proteins.[50] The observed confined diffusion may be a result of protein-protein interactions (as discussed below for ion channels), anchoring to the cytoskeleton, lipid microdomains, or spatial partitioning of the plasma membrane, as recently demonstrated for the neuronal surface.[69–73]

We have previously revealed the interaction of BACE1 with the voltage-gated sodium channel $Na_V1.2$, voltage-gated potassium channel $K_V3.4$, and potassium channels of the KCNQ family (KCNQ1-3), for which BACE1 acts as a non-proteolytic accessory

subunit.[22,74-77] Both $Na_V1.2$ and KCNQ2/3 are anchored to the actin cytoskeleton at the axon initial segment by interaction with ankyrin-G.[78] A similar anchoring to actin has been described for KCNQ1 via the protein kinase A anchoring protein (AKAP) yotiao.[50,79] It is therefore conceivable that the restricted motility of BACE1 results, at least in part, from its physical association with anchored membrane proteins. In future studies, tracking BACE1 diffusion with **SiR-BACE1** might offer a means to identify putative new interaction partners and regulators of the secretase.

Membrane composition and protein surface diffusion has garnered increasing attention in AD research.[80] For instance, increased cholesterol levels support encounters of BACE1 with APP in membrane subdomains, facilitating joint endocytosis and APP processing.[81,82] *Vice versa*, membrane partitioning can preclude protease-substrate interaction, as demonstrated for ADAM10 and its chemokine substrate CX3CL1.[83] This raises the question of whether the efficacy of BACE1 inhibitors depends on membrane composition and sub-cellular BACE1 localization. In a successful attempt to optimize inhibition, the pharmacophore was directed towards endosomes, where BACE1 is located, active, and in a protonation state favoring drug binding.[84,85] Just as well, membrane partitioning and protein confinement could determine an inhibitor's potency already at the cell surface. Remarkably, clustering of target molecules has been discussed to allow enzymatic reaction bursts despite the presence of high doses of inhibitors.[86]

In conclusion, we have introduced **SiR-BACE1** as new tool for live cell imaging of BACE1. The probe should become valuable for monitoring the distribution and dynamics of BACE1 in cellular membranes and the development of AD therapeutics that aim to either modulate the membrane to prevent BACE1-APP interaction or target inhibitors to the protease.

Experimental Section

Chemistry

All compounds used in the results section **(13a-f)** were determined to be >95% pure by analytical HPLC. All chemical reagents and anhydrous solvents for synthesis were purchased from commercial suppliers (Sigma-Aldrich, Fluka, Acros, Fluorochem, TCI) and were used without further purification or distillation. If necessary, solvents were degassed either by freeze-pump-thaw or by bubbling N_2 through the vigorously stirred solution for several minutes.

NMR spectra were recorded in deuterated solvents on a BRUKER DPX 400 or on a BRUKER DPX 400 instruments and calibrated to residual solvent peaks ($^1H/^{13}C$ in ppm): $CDCl_3$ (7.26/77.00), DMSO-d_6 (2.50/39.52), acetone-d_6 (2.05). Multiplicities are abbreviated as follows: s = singlet, d = doublet, t = triplet, q = quartet, p = pentet, br = broad, m = multiplet. Coupling constants *J* are reported in Hz. Spectra are reported based on appearance, not on theoretical multiplicities derived from structural information.

High-resolution mass spectra (HRMS) were measured on a Micromass Q-TOF Ultima spectrometer with electrospray ionization (ESI).

LC-MS was performed on a Shimadzu MS2020 connected to a Nexerra UHPLC system equipped with a Waters ACQUITY UPLC BEH C18 1.7 µm 2.1x50 mm column. Buffer A: 0.05% HCOOH in H_2O Buffer B: 0.05% HCOOH in acetonitrile. Analytical gradient was from 10% to 90% B within 5.0 min with 0.5 or 1.0 mL/min flow.

Preparative RP-HPLC was performed on a Dionex system equipped with an UVD 170U UV-Vis detector for product visualization on a Waters SunFireTM Prep C18 OBDTM 5 µm 10×150 mm column. Buffer A: 0.1% TFA in H_2O Buffer B: acetonitrile. Typical gradient was from 10% to 90% B within 32 min with 4 mL/min flow. After lyophilization of HPLC-purified compounds, the solid residue was generally dissolved in dry DMSO and the

concentration of the SiR-derivatives was measured by UV-Vis spectroscopy in PBS containing 0.1% SDS, using the SiR molar extinction coefficient of 100,000 $M^{-1}cm^{-1}$ at 650 nm.

Flash column chromatography was performed on a Teledyne ISCO CombiFlash® Rf+ with pre-packed silica columns or manually on silica gel (SilicaDlash® P60, 0.040–0.063 mm, 230-400 mesh, Silicycle). Reactions and chromatography fractions were monitored by thin layer chromatography (TLC) on Merck silica gel 60 F254 glass plates. The spots were visualized either under UV light at 254 nm and/or 366 nm.

4-Bromo-2,6-diethylpyridine (Figure 1C, 3)

4-Bromo-2,6-diethylpyridine was prepared as previously described[40] from 1,3-acetonedicarboxylic acid (**1**) and propionic anhydride (**2**) over five steps and obtained as a yellow to colorless light oil in 0.8% yield.

^{1}H NMR (400 MHz, $CDCl_3$): δ [ppm] = 7.15 (s, 2H), 2.76 (q, J = 7.6 Hz, 4H), 1.28 (t, J = 7.6 Hz, 6H).

^{13}C NMR (101 MHz, $CDCl_3$): δ [ppm] = 164.4, 133.3, 122.3, 31.3, 13.9.

HRMS (ESI): calc. for $C_9H_{13}BrN$ $[M+H]^+$: 214.0226 and 216.0205, found: 214.0230 and 216.0211.

R_f (TLC; hexanes/DCM = 1/1) = 0.42.

3,7-Bis(dimethylamino)-N-(3-guanidinoalkyl)-5,5-dimethyl-3'-oxo-3'H,5H-spiro[dibenzo[b,e]siline-10,1'-isobenzofuran]-6'-carboxamide (5a-f)

General procedure: A 2 mL vial was charged with SiR-6-COOH **4** (1.0 equiv.) in DMSO (1 mL / 10 mg SiR-6-COOH) and DIPEA (4.0 equiv.) and TSTU (1.2 equiv.) was added in one portion. Upon addition, the mixture turned from blue to colorless (DIPEA) to yellow (TSTU). After stirring at rt for 5 min, 1,n-diaminoalkane (10 equiv.) was added (liquid diamines were

pipetted directly into the solution while solids were dissolved in a minimal amount of DMSO and then added in one portion) and the reaction mixture was vigorously stirred for 1 h (turning colorless) it was quenched with HOAc (25 equiv.) and 0.1% aqueous TFA (200 µL / 10 mg SiR-6-COOH) and the crude subjected to RP-HPLC ($MeCN/H_2O/TFA$ = 10/90/0.1 → 90/10/0.1 over 32 minutes). The desired monoamine was collected (λ = 650 nm), freeze-dried and the obtained blue powder was dissolved in DMF (1 mL / 10 mg SiR-6-COOH) and NEt_3 (15 equiv.) before 1*H*-pyrazole-1-carboximidamide hydrochloride (10 equiv.) was added in one portion. The reaction mixture was vigorously stirred for 2 h before it was quenched with HOAc (20 equiv.) and the crude subjected to RP-HPLC ($MeCN/H_2O/TFA$ = 10/90/0.1 → 90/10/0.1 over 32 minutes). The obtained guanidine was freeze-dried to obtain the desired product as a blue powder and briefly characterized by LC-MS analysis ($MeCN/H_2O$/formic acid = 10/90/0.1 → 100/10/0.1 over 6 min).

3,7-Bis(dimethylamino)-*N*-(3-guanidinobutyl)-5,5-dimethyl-3'-oxo-3'*H*,5*H*-spiro[dibenzo[*b*,*e*]siline-10,1'-isobenzofuran]-6'-carboxamide (n = 4, **5c**) was obtained in 85% yield over 2 steps and subjected to further ^{1}H NMR and HRMS characterization:

^{1}H NMR (400 MHz, acetone-d_6): δ [ppm] = 8.47 (s, 1H), 8.24 (s, 1H), 8.15 (dd, J = 10.3, 7.6 Hz, 1H), 8.06–7.91 (m, 1H), 7.82–7.74 (m, 1H), 7.49 (br s, 3H), 7.20–7.11 (m, 2H), 6.83–6.74 (m, 2H), 6.71–6.65 (m, 2H), 3.43 (t, *J* = 5.3 Hz, 2H), 3.40–3.28 (m, 2H), 2.99 (s, 12H), 1.70–1.66 (m, 4H), 0.68 (s, 3H), 0.55 (s, 3H).

HRMS (ESI): calc. for $C_{32}H_{41}N_6O_3Si$ $[M+H]^+$: 585.3004, found: 585.3004.

3-(3-Bromophenyl)-2-fluoropyridine (8)

A Schlenk flask was charged with (2-fluoropyridin-3-yl)boronic acid (**6**) (249 mg, 1.77 mmol, 1.0 equiv.), 1-bromo-3-iodobenzene (**7**) (500 mg, 1.77 mmol, 1.0 equiv.) and Cs_2CO_3 (577 mg, 1.77 mmol, 1.0 equiv.) suspended in DME / H_2O (8 mL / 2 mL). The suspension was degassed by bubbling with nitrogen for 10 min under stirring before $Pd(PPh_3)_4$ (204 mg,

0.177 mmol, 0.1 equiv.) was added in one portion. The flask was sealed and the reaction mixture was heated to 85 °C to become homogenous and stirred for 18 h before it was allowed to cool to rt and then quenched by the addition of water (100 mL) and extracted with EtOAc (2 x 100 mL). The combined organic layers were washed with water (100 mL) and brine (100 mL), dried over $MgSO_4$ and the volatiles were removed *in vacuo*. The crude was taken up in DCM and hexanes was added to precipitate the majority of PPh_3 that was filtered off before the solution was subjected to FCC (80 g silica: 3 CV 100% hexanes → 10 CV gradient to 100% DCM → 1 CV 100% DCM; the product eluted ~90% DCM) to obtain 88.0 mg (0.350 mmol) of the desired product as a clear oil in 20% yield.

^{1}H NMR (400 MHz, $CDCl_3$): δ [ppm] = 8.20 (dt, J = 4.9, 1.6 Hz, 1H), 7.83 (ddd, J = 9.6, 7.4, 2.0 Hz, 1H), 7.69 (d, J = 1.7 Hz, 1H), 7.52 (ddd, J = 8.0, 2.0, 1.0 Hz, 1H), 7.50–7.46 (m, 1H), 7.32 (t, J = 7.9 Hz, 1H), 7.27 (ddd, J = 7.5, 4.9, 1.8 Hz, 1H).

^{13}C NMR (101 MHz, $CDCl_3$): δ [ppm] = 160.1 (d, J = 240.5 Hz), 146.9 (d, J = 14.7 Hz), 140.5 (d, J = 4.1 Hz), 135.8 (d, J = 5.1 Hz), 131.6 (d, J = 3.1 Hz), 131.4, 130.1, 127.4 (d, J = 3.3 Hz), 122.6, 122.3 (d, J = 28.3 Hz), 121.9 (d, J = 4.4 Hz).

^{19}F NMR (376 MHz, $CDCl_3$): δ [ppm] = –70.73 (d, J = 9.7 Hz).

HRMS (ESI): calc. for $C_{11}H_8BrFN$ $[M+H]^+$: 251.9819 and 253.9798, found: 251.9823 and 253.9804.

UV/Vis (LCMS): λ_{max1} = 226 nm; λ_{max2} = 268 nm.

t_R (LCMS; MeCN/H_2O/formic acid = 10/90/0.1 → 90/10/0.1 over 6 min) = 3.900 min.

R_f (TLC; hexanes/DCM = 1/1) = 0.41.

2-Fluoro-3-(3-((trimethylsilyl)ethynyl)phenyl)pyridine (9)

A Schlenk flask was charged with 3-(3-bromophenyl)-2-fluoropyridine (**8**) (302 mg, 1.20 mmol, 1.0 equiv.), TMS-acetylene (141 mg, 1.44 mmol, 205 µL, 1.2 equiv.), CuI (2.2 mg, 12 µmol, 0.01 equiv.) and $PdCl_2(PPh_3)_2$ (25 mg, 36 µmol, 0.03 equiv.) dissolved in degassed

DMF / NEt_3 (5 mL / 1 mL) under a nitrogen atmosphere. The reaction mixture was heated to 65 °C o.n. before it was allowed to cool to rt and quenched by the addition of water (50 mL) and extracted with EtOAc (50 mL). The organic layer was washed with water (2 x 100 mL) and brine (100 mL), dried over $MgSO_4$ and the solvents were removed *in vacuo*. The crude was subjected to FCC (40 g silica: 2 CV 100% hexanes → 10 CV gradient to 100% DCM → 3 CV 100% DCM; the product eluted ~85% DCM) to obtain 251 mg (0.93 mmol) of the desired product as a yellow oil in 78% yield.

^{1}H NMR (400 MHz, $CDCl_3$): δ [ppm] = 8.18 (ddd, J = 4.9, 1.9, 1.1 Hz, 1H), 7.83 (ddd, J = 9.6, 7.4, 2.0 Hz, 1H), 7.64 (q, J = 1.6 Hz, 1H), 7.51–7.47 (m, 2H), 7.42–7.35 (m, 1H), 7.29–7.21 (m, 1H), 0.25 (s, 9H).

^{13}C NMR (101 MHz, $CDCl_3$): δ [ppm] = 160.2 (d, J = 240.3 Hz), 146.6 (d, J = 14.7 Hz), 140.6 (d, J = 4.2 Hz), 133.9 (d, J = 5.0 Hz), 132.1 (d, J = 2.6 Hz), 131.7, 128.8 (d, J = 3.3 Hz), 128.6, 122.9 (d, J = 28.3 Hz), 121.8 (d, J = 4.5 Hz), 104.3, 94.9, –0.2.

^{19}F NMR (376 MHz, $CDCl_3$): δ [ppm] = –70.9 (d, J = 9.8 Hz).

HRMS (ESI): calc. for $C_{16}H_{17}FNSi$ $[M+H]^+$: 270.1109, found: 270.1111.

UV/Vis (LCMS): λ_{max1} = 244 nm; λ_{max2} = 257 nm.

t_R (LCMS; MeCN/H_2O/formic acid = 10/90/0.1 → 90/10/0.1 over 6 min) = 4.897 min.

R_f (TLC; hexanes/DCM = 1/1) = 0.45.

3-(3-Ethynylphenyl)-2-fluoropyridine (10)

A round bottom flask was charged with 2-fluoro-3-(3-((trimethylsilyl)ethynyl)phenyl)pyridine (**9**) (251 mg, 0.93 mmol, 1.0 equiv.) and Cs_2CO_3 (363 mg, 1.12 mmol, 1.2 equiv.) dissolved in EtOH / DCM (10 mL / 10 mL) and stirred at rt for 30 min. The volatiles were removed *in vacuo* and the crude was filtered through a plug of silica with DCM to obtain 180 mg (0.91 mmol) of the desired product as an orange-brown oil in 98% yield.

^{1}H NMR (400 MHz, $CDCl_3$): δ [ppm] = 8.18 (dt, J = 4.9, 1.6 Hz, 1H), 7.83 (ddd, J = 9.6, 7.4, 2.0 Hz, 1H), 7.66 (q, J = 1.6 Hz, 1H), 7.54–7.49 (m, 2H), 7.40 (t, J = 7.8 Hz, 1H), 7.31–7.20 (m, 1H), 3.11 (s, 1H).

^{13}C NMR (101 MHz, $CDCl_3$): δ [ppm] = 160.2 (d, J = 240.4 Hz), 146.6 (d, J = 14.7 Hz), 140.5 (d, J = 4.3 Hz), 134.0 (d, J = 5.0 Hz), 132.2 (d, J = 2.9 Hz), 131.9, 129.1 (d, J = 3.3 Hz), 128.7, 122.9, 122.6, 121.8 (d, J = 4.5 Hz), 82.9, 77.8.

^{19}F NMR (376 MHz, $CDCl_3$): δ [ppm] = –70.9 (d, J = 9.7 Hz).

HRMS (ESI): calc. for $C_{13}H_9FN$ $[M+H]^+$: 198.0714, found: 198.0717.

UV/Vis (LCMS): λ_{max1} = 229 nm; λ_{max2} = 268 nm.

t_R (LCMS; MeCN/H_2O/formic acid = 10/90/0.1 → 90/10/0.1 over 6 min) = 3.618 min.

R_f (TLC; hexanes/DCM = 1/1) = 0.39.

2,6-Diethyl-4-((3-(2-fluoropyridin-3-yl)phenyl)ethynyl)pyridine (11)

A Schlenk flask was charged with 3-(3-ethynylphenyl)-2-fluoropyridine (**10**) (180 mg, 0.91 mmol, 1.0 equiv.), 4-bromo-2,6-diethylpyridine (196 mg, 0.91 mmol, 1.0 equiv.), CuI (1.7 mg, 9.1 µmol, 0.01 equiv.) and $PdCl_2(PPh_3)_2$ (19.2 mg, 27.3 µmol, 0.03 equiv.) dissolved in degassed DMF / NEt_3 (5 mL / 1 mL) and flushed with nitrogen. The reaction mixture was heated to 65 °C o.n. before it was allowed to cool to rt and quenched by the addition of water (50 mL) and extracted with EtOAc (50 mL). The organic layer was washed with water (2 x 100 mL) and brine (100 mL), dried over $MgSO_4$ and the solvents were removed *in vacuo*. The crude was subjected to FCC (40 g silica: 20 CV 20% EtOAc/hexanes) to obtain 199 mg (0.60 mmol) of the desired product as a light-yellowish oil in 66% yield.

^{1}H NMR (400 MHz, $CDCl_3$): δ [ppm] = 8.27–8.15 (m, 1H), 7.88 (ddd, J = 9.6, 7.4, 1.9 Hz, 1H), 7.74 (q, J = 1.6 Hz, 1H), 7.58–7.55 (m, 2H), 7.46 (t, J = 7.7 Hz, 1H), 7.31–7.26 (m, 1H), 7.10 (s, 2H), 2.80 (q, J = 7.6 Hz, 4H), 1.30 (t, J = 7.6 Hz, 6H).

^{13}C NMR (101 MHz, $CDCl_3$): δ [ppm] = 163.2, 160.3 (d, J = 240.4 Hz), 146.8 (d, J = 14.6 Hz), 140.6 (d, J = 4.2 Hz), 134.3 (d, J = 5.0 Hz), 132.1 (d, J = 2.9 Hz), 131.7, 131.5, 129.3 (d, J = 3.2 Hz), 128.9, 123.1, 122.9 (d, J = 28.2 Hz), 121.9 (d, J = 4.5 Hz), 120.9, 91.8, 88.2, 31.4, 14.0.

^{19}F NMR (376 MHz, $CDCl_3$): δ [ppm] = –70.8 (d, J = 9.8 Hz).

HRMS (ESI): calc. for $C_{22}H_{20}FN_2$ $[M+H]^+$: 331.1605, found: 331.1632.

UV/Vis (LCMS): λ_{max1} = 225 nm; λ_{max2} = 277 nm, λ_{max3} = 302 nm, λ_{max4} = 321 nm.

t_R (LCMS; MeCN/H_2O/formic acid = 10/90/0.1 → 90/10/0.1 over 6 min) = 3.178 min.

R_f (TLC; hexanes/EtOAc = 8/2) = 0.26.

1-(2,6-Diethylpyridin-4-yl)-2-(3-(2-fluoropyridin-3-yl)phenyl)ethane-1,2-dione (12)

A round bottom flask was charged with 2,6-diethyl-4-((3-(2-fluoropyridin-3-yl)phenyl)ethynyl)pyridine (**11**) (199 mg, 0.60 mmol, 10 equiv.) dissolved in acetone (20 mL). $NaHCO_3$ (30 mg, 0.36 mmol, 0.6 equiv.) and $MgSO_4$ (108 mg, 0.90 mmol, 1.5 equiv.) was added to the solution to obtain a slurry, to which $KMnO_4$ (209 mg, 1.32 mmol, 2.2 equiv.) was added spatula-wise at rt. The reaction mixture was warmed to and stirred at 40 °C for 1 h before it was diluted with water (100 mL) and extracted with Et_2O (2 x 100 mL). The combined organic layer was washed with water (100 mL) and brine (100 mL), dried over $MgSO_4$ and the solvents were removed *in vacuo*. The crude was subjected to FCC (40 g silica: 2 CV 10% EtOAc/hexanes → 5 CV gradient to 50% EtOAc/hexanes → 5 CV 50% EtOAc/hexanes) to obtain 73 mg (0.20 mmol) of the desired product as a yellow wax in 34% yield.

^{1}H NMR (400 MHz, $CDCl_3$): δ [ppm] = 8.23 (ddd, J = 4.9, 1.9, 1.2 Hz, 1H), 8.17–8.15 (m, 1H), 7.98 (dt, J = 7.8, 1.4 Hz, 1H), 7.92–7.87 (m, 2H), 7.63 (t, J = 7.8 Hz, 1H), 7.44 (s, 2H), 7.30 (ddd, J = 7.4, 4.9, 1.7 Hz, 1H), 2.86 (q, J = 7.6 Hz, 4H), 1.29 (t, J = 7.6 Hz, 6H).

^{13}C NMR (101 MHz, $CDCl_3$): δ [ppm] = 193.4, 192.2, 164.5, 159.8 (d, J = 240.4 Hz), 146.9 (d, J = 14.7 Hz), 140.3 (d, J = 3.9 Hz), 139.2, 135.0 (d, J = 3.6 Hz), 134.8 (d, J = 5.1 Hz), 132.7, 129.6, 129.6 (d, J = 2.5 Hz), 129.2, 121.9 (d, J = 28.5 Hz), 121.7 (d, J = 4.5 Hz), 117.4, 31.2, 13.5.

^{19}F NMR (376 MHz, $CDCl_3$): δ [ppm] = –71.0 (d, J = 9.7 Hz).

HRMS (ESI): calc. for $C_{22}H_{20}FN_2O_2$ $[M+H]^+$: 363.1503, found: 363.1504.

UV/Vis (LCMS): λ_{max1} = 234 nm; λ_{max2} = 265 nm.

t_R (LCMS; MeCN/H_2O/formic acid = 10/90/0.1 → 90/10/0.1 over 6 min) = 4.086 min.

R_f (TLC; hexanes/EtOAc = 8/2) = 0.16.

4-((3-(2-Amino-4-(2,6-diethylpyridin-4-yl)-4-(3-(2-fluoropyridin-3-yl)phenyl)-5-oxo-4,5-dihydro-1H-imidazol-1-yl)alkyl)carbamoyl)-2-(7-(dimethylamino)-3-(dimethyliminio)-5,5-dimethyl-3,5-dihydrodibenzo[b,e]silin-10-yl)benzoate (13a-f)

All SiR647-linked BACE1 inhibitors were firstly synthesized on a <0.5 mg scale for initial biological assessment and only the C4 linker (*i.e.* SiR-BACE1) was upscaled.

General procedure: A vial was charged with SiR-guanidine **5** (1.0 equiv.), 1-(2,6-diethylpyridin-4-yl)-2-(3-(2-fluoropyridin-3-yl)phenyl)ethane-1,2-dione (**12**) (1.0 equiv.) dissolved in EtOH / 1,4-dioxane / H_2O (0.5 / 0.4 / 0.1, V_{tot} = 1 mL / 0.5 mg **5**). Na_2CO_3 was added spatula tip-wise until the color changed from blue to pale yellow forming the spirolactone before the reaction mixture was heated to 85 °C for 1 h. The reaction was quenched with HOAc (10 equiv.) and the crude subjected to RP-HPLC (MeCN/H_2O/TFA = 10/90/0.1 → 90/10/0.1 over 32 minutes). The obtained probe was freeze-dried to obtain the desired product as a blue powder.

4-((3-(2-Amino-4-(2,6-diethylpyridin-4-yl)-4-(3-(2-fluoropyridin-3-yl)phenyl)-5-oxo-4,5-dihydro-1*H*-imidazol-1-yl)butyl)carbamoyl)-2-(7-(dimethylamino)-3-(dimethyliminio)-5,5-

dimethyl-3,5-dihydrodibenzo[*b*,*e*]silin-10-yl)benzoate (n = 2, **13c**, SiR-BACE1) was obtained in 93% yield and subjected to further ^{1}H NMR characterization:

^{1}H NMR (400 MHz, acetone-d_6): δ [ppm] = 8.26 (t, *J* = 5.8 Hz, 1H), 8.23 (d, *J* = 4.9 Hz, 1H), 8.08 (ddd, *J* = 9.7, 7.8, 1.8 Hz, 2H), 8.01 (d, *J* = 8.0 Hz, 1H), 7.79 (s, 1H), 7.74 (d, *J* = 1.3 Hz, 1H), 7.69 (dd, *J* = 6.7, 2.0 Hz, 1H), 7.63–7.54 (m, 4H), 7.40 (ddd, *J* = 7.0, 4.8, 1.8 Hz, 1H), 7.16 (d, *J* = 2.8 Hz, 2H), 6.78 (d, *J* = 8.9 Hz, 2H), 6.68 (dd, *J* = 9.0, 2.9 Hz, 2H), 3.95 (dd, *J* = 8.7, 6.5 Hz, 2H), 3.43 (t, *J* = 6.2 Hz, 2H), 3.01 (s, 12H), 2.91 (q, *J* = 7.6 Hz, 4H), 1.77 (q, *J* = 7.4 Hz, 2H), 1.67 (q, *J* = 7.1 Hz, 2H), 1.26 (t, *J* = 7.6 Hz, 6H), 0.68 (s, 3H), 0.55 (s, 3H).

Purity for all compounds **13a-f** was assessed by analytical HPLC (Waters e2695 HPLC system equipped with a Supelco Ascentis C18 5.0 µm 250x10 mm column. Buffer A: 0.1% TFA in dH_2O Buffer B: 0.1% TFA in MeCN. Analytical gradient was: 10% B for 5.0 min; from 10% to 90% within 30.0 min; 90% B for 5.0 min; from 90% to 95% within 4.0 min; 95% for 1.0 min with either 4.0 mL/min flow, absorbance was monitored at λ = 648 nm), as displayed in Supplementary Figure 1.

Animals

BACE1$^{-/-}$ mice (BACE1^{tm1Psa}) were generated by insertion of a neo cassette into exon 1 of the *Bace1* gene, resulting in a premature translational stop codon.[87] Mice had *ad libitum* access to food and water and were housed and fed according to federal guidelines. Genotyping was performed by PCR amplification for detection of wild type allele or neo cassette.

Plasmids

hBACE1 (NM_012104.4) and hBACE1(D289N), both kindly provided by Michael Willem (Adolf-Butenandt-Institute, Ludwig-Maximilians-Universität München, Germany), hBACE2 (NM_012105.3), and h-cathepsinD (HsCD00438327, Harvard PlasmID, Harvard Medical

School, Boston, MA, USA) were all fused to EGFP (U55761.1) in pcDNA3.1 hygro+ (Thermo Fisher Scientific). hBACE1 was additionally sub-cloned in pcDNA3.1 hygro+ without addition of a tag (referred to as "untagged hBACE1"), and sub-cloned in pcDNA3.1 hygro+ with insertion of SNAP tag (from pSNAPf, NEB) after its pro-peptide following amino acid 45 to generate SNAP-hBACE1. Membrane localization signal (Mls) from Fyn kinase[88] was fused to EGFP in pcDNA3.1 hygro+ to generate Mls-EGFP.

Cell lines

HEK293T cells (ATCC accession number CRL-11268) were maintained in DMEM with 1 g/l glucose (Sigma-Aldrich D6046), supplemented with 10% FCS (Merck) and 1% penicillin/streptomycin (PAA); N1E-115 murine neuroblastoma cells (ATCC: CRL-2263) in DMEM with 4.5 g/l glucose (Thermo Fisher Scientific D5796), supplemented with 10% FCS and 1% pen/strep; and CHO-K1 cells (ATCC: CCL-61) in RPMI without phenol red (Sigma-Aldrich R7509), supplemented with 10% FCS and 2 mM L-glutamine (Sigma-Aldrich). Mouse embryonic fibroblasts (MEF) were prepared from BACE1 knockout mice (kindly provided by Karina Reiß, Department of Dermatology and Allergology, University Hospital Schleswig-Holstein, Campus Kiel, Germany). MEF were cultured in DMEM with 4.5 g/l glucose (Thermo Fisher Scientific D5796), supplemented with 10% FCS and 1% pen/strep. All cells were cultured at 37 °C, 5% CO_2.

Fluorescence spectra

Absorption of **SiR-BACE1** was measured at 137 µM with a Nanodrop 2000 (Thermo Fisher Scientific) in PBS or PBS/0.2% SDS (C. Roth) with a resolution of 1 data point per 1 nm. Emission was recorded at 10 µM in PBS/0.2% SDS with a Tecan Infinite M1000 (Tecan) at 1 data point per 2 nm or at 100 nM in HBS pH 5 in the absence or presence of 200 nM

recombinant mouse BACE1 protein (amino acids 1-457, equaling the extracellular domain (ECD), Thermo Fisher Scientific 50002M08H50) with TECAN Spark M20 plate reader at 1 data point per 1 nm.

Buffers

HEPES-buffered saline (HBS) contained, in mM: 150 NaCl, 3 KCl, 2 $CaCl_2$, 2 $MgCl_2$, 10 HEPES, 10 D-glucose, adjusted to pH 5, pH 7.4, or pH 8 (with HCl or NaOH), as stated in the results. Plasma membrane lawn (PML) buffer contained, in mM: 70 KCl, 30 HEPES, 5 $MgCl_2$, 3 EGTA, adjusted to pH 7.5. Chemicals were purchased from Sigma-Aldrich, C. Roth, and Merck.

Confocal laser scanning microscopy

Confocal imaging was performed with an inverse Zeiss Axio Observer.Z1 equipped with the LSM 780 module, 405 nm laser diode, LASOS argon laser LGN 3001 for 488 nm laser line, HeNe633 laser, HAL 100 transmitted-light illumination, Plan-Apochromat 63x/1.40 Oil DIC objective, Plan-Apochromat 20x/0.8 objective, and ZEN 2010 software.

HEK293T cells were plated onto sterile 18 mm 1.5H borosilicate coverslips (VWR) and transfected 1 d later using jetPEI (Polyplus-transfection). After 1 d, cells were used for evaluation of linker length, pH dependency, and BACE1-specific labeling. All live cell imaging was performed with the 63x objective and the pinhole set to 1 AU for each channel.

For linker length evaluation, live cells were washed twice with HBS pH 5 and stained with 100 nM solutions of the conjugates in HBS pH 5 at room temperature for 20 min. Cells were then incubated in HBS pH 5 for imaging. ZEN software was used to generate 3-pixel averages for colocalization analysis. Colocalization scatter plots were generated for whole frames and

for representative regions of interest (ROIs) covering the plasma membrane or intracellular clusters.

For evaluation of pH dependency, cells were stained as either live or fixed samples. Live cells were washed with HBS and stained with 100 nM **SiR-BACE1** in HBS for 2 min at 4 °C. HBS was either used at pH 5 or pH 7.4. Confocal images were acquired in HBS pH 7.4. For fixation, cells were washed twice with PBS and treated with 4% PFA (C. Roth), 1.44% Na_2HPO_4 x 2 H_2O (C. Roth), 0.26% NaH_2PO_4 x 1 H_2O (Merck) for 10 min at room temperature. Next, cells were washed twice with PBS and once with HBS pH 7.4, stained with 100 nM **SiR-BACE1** in HBS pH 7.4 for 10 min at 4 °C, washed twice with HBS pH 7.4, and subjected to confocal time-lapse imaging in HBS pH 7.4 with the 63x objective and the pinhole set to 1 AU for each channel. EGFP and SiR intensity were monitored over 2 h with an interval of 3 min. Medium was changed to HBS pH 5 after 60 min.

For evaluation of BACE1-specific labeling, cells were washed with HBS pH 5 and stained with 100 nM **SiR-BACE1** in HBS pH 5 for 2 min at 4 °C. Confocal imaging was done in HBS pH 7.4.

Overview images for STED samples were acquired with the 20x objective. For display, fluorescence channels were registered in Fiji[89] using the StackReg plugin.

BACE1 activity FRET assay

Inhibition of BACE1 proteolytic activity was tested for conjugates of all linker lengths with a fluorescence resonance energy transfer (FRET)-based BACE1 assay (Thermo Fisher Scientific; P2985). Despite overlapping TMR emission and SiR excitation spectra, we observed no confounding FRET between those two fluorophores. Inhibition was determined in endpoint assays according to the manufacturer's protocol, using black 384-well plates (Greiner) with total reaction volume reduced to 12 µl. Fluorescence was quantified with a Tecan Infinite M1000 reader with a Quad4 monochromator (Tecan). Experiments were done

in triplicate and each plate was quantified three times to obtain 9 data points per concentration. Product fluorescence (I) as a function of conjugate concentration (c) was fitted to a logistic curve in OriginPro per the following equation:

$$I(c) = \frac{I_1 - I_2}{1 + \left(\frac{c}{IC_{50}}\right)^p} + I_2 \qquad \textit{Equation 1}$$

with I_1 and I_2 being the initial and final asymptotes and p being the power. k-means cluster analysis of IC_{50} was performed with k = 2 and subsequent ANOVA testing in OriginPro. For analysis of pH effects, assay buffer was replaced by HBS pH 5, 7.4, or 8, and incubation was extended to over-night. Assay activity was determined by subtracting I_2 from I_1.

Fluorescence correlation spectroscopy (FCS)

In Small Volume Sensoplates (Greiner 788896), **SiR-BACE1** in HBS pH 5 or 7.4 was mixed with recombinant mouse BACE1 protein (amino acids 1-457, equaling the extracellular domain (ECD), Thermo Fisher Scientific 50002M08H50), which had been dissolved in H_2O. FCS was performed with the LSM 780 with 10% power of the 50 mW 633 nm laser line and a C-Apochromat 40x/1.20 objective selected for FCS with water immersion at 22 ± 1 °C approx. 50 µm above the glass surface. Pinhole was set to 1 AU and calibrated before every session. The correction collar and positioning of the plate were adjusted to optimize photon yield. SiR intensity was recorded from a point scan at 20 MHz for 500x (time-lapse) or 30x (end-point FCS) 10 s at 647-691 nm with the GaAsP array. Data were auto-correlated and fitted with Zeiss' 1- or 2-component 3D translational models, both additionally considering a triplet state, in ZEN2010 with the FCS software module. For time-lapse FCS recordings, data were displayed as 6-point adjacent averages equaling sampling intervals of 1 min. Parameterized time-lapse data of slowly diffusing **SiR-BACE1** (J) over time (t) were fitted to the exponential curve

$$J(t) = J_\infty + A \times 2^{-t/t_{0.5}} \qquad \textit{Equation 2}$$

with J_∞ being the asymptote and A being the amplitude or to a linear curve with slope set to 0. Parameterized data from end-point FCS recordings were fitted to logistic curves (Equation 1).

Flow cytometry

HEK293T cells were cultured in 12-well plates and transfected with hBACE1-EGFP using jetPEI (Polyplus-transfection). After 1 d, cells were washed with HBS pH 5 and stained with **SiR-BACE1** in HBS pH 5 for 2 min at 4 °C. For a second data set, cells were stained with 70 nM **SiR-BACE1** in HBS pH 5, containing different concentrations of BACE1 inhibitor IV (Merck, Calbiochem), for 2 min at 4 °C. After staining, cells were washed with HBS pH 7.4, detached with accutase (PAA), resuspended in phenol red-free RPMI / 10% FCS / 2 mM L-glutamine, and pelletized by centrifugation. Cells were resuspended in 1 mL flow cytometry buffer (5 mM EDTA x 2 H_2O (Merck), 2% FCS in PBS) and analyzed with a Cytoflex S (Beckman Coulter) equipped with 488 nm and 638 nm laser lines, and 525/40 BP and 660/20 BP detection filters at a sample flow rate of 30 µl/s. Data was collected and analyzed with CytExpert 1.2 software (Beckman Coulter). Living cells were identified per size and granularity according to forward and sideward scatter, respectively. 35,000 living cells were measured per recording. Fluorescence data was exported with FCSExtract 1.02 (Earl F Glynn, Stowers Institute for Medical Research, Kansas City, Missouri, USA), and **SiR-BACE1** intensity ($I_{SiR\text{-}BACE1}$) as a function of EGFP intensity (I_{EGFP}) was fitted to a bilinear custom equation programmed in Origin C:

$$I_{SiR-BACE1} = \begin{cases} m \times A + I_0 & for\ I_{EGFP} \leq A \\ m \times I_{EGFP} + I_0 & for\ I_{EGFP} > A \end{cases} \qquad \textit{Equation 3}$$

with A being the EGFP intensity at which the curve switches from the horizontal to the ascending part, and m and I_0 being the slope (proportionality factor) or intercept of the

ascending part, respectively. A, m, and I_0 were determined by the fit. EC_{50} for **SiR-BACE1** staining and IC_{50} for inhibitor IV competition were determined by fitting m to a logistic curve (Equation 1).

Stimulated emission depletion microscopy (STED)

N1E-115 cells were seeded onto sterile 18 mm 1.5H borosilicate coverslips (VWR), which had been previously coated with 0.1 mg/mL poly-D-lysine (Sigma-Aldrich) for 20 min, and were maintained in culture medium for 1 d. Cells were transfected with 500-800 ng hBACE1-EGFP using jetPRIME (Polyplus-transfection SA). Just before transfection, medium was changed to induction medium (DMEM supplemented with 2% FCS, 1,25% DMSO, 1% pen/strep), in which cells were kept for 3 d.

Before staining, cells were washed twice with PBS, fixed with 4% PFA (see above) for 10 min at room temperature, washed twice with PBS and once with HBS pH 5. Staining was accomplished with 100 nM **SiR-BACE1** in HBS pH 5 for 10 min at room temperature, followed by washing twice with HBS pH 5 and mounting with Fluoromount G (Electron Microscopy Sciences) and Twinsil (picodent).

Super-resolution imaging was performed at the Optical Imaging Centre Erlangen (OICE) with an Abberior Stimulated Emission Depletion (STED) setup based on an inverse Olympus IX83 equipped with a 100x/1.44 oil immersion objective, pulsed 485 nm and 640 nm excitation lasers, pulsed 1.2 W 775 nm depletion laser, ET525/50 and ET685/70 emission filters, and APD detectors. Data were acquired at 16-bit with a pixel size of 50 nm and 100 line averages, using the STED laser at 50% and the pinhole at 1.2 AU with Imspector software. Representative profiles were extracted in Fiji from 3-pixels-wide ROIs over corresponding structures in STED and confocal image.

Imaging of endogenous BACE1

At postnatal age of 33 days (p33), wild type and knockout mice were anesthetized with Sevofluran (Sevorane, AbbVie) and decapitated. Brains were dissected, covered with Tissue-Tek (Sakura Finetek), and frozen at -40 °C in methylbutan (C. Roth) for 1-2 min. Tissue was sliced into 14 µm coronal sections, which were placed on polysine slides (R. Langenbrinck), and stored at -20 °C until use. For staining, slices were thawed shortly, rehydrated with PBS, and circumvented with silicone grease (VWR) to minimize staining area. Tissue was preincubated for 45 min with PBS / 5% bovine serum albumin (BSA, Sigma-Aldrich) at room temperature before staining with 1 µM **SiR-BACE1** in HBS pH 5 for 1 h at 4 °C in the presence or absence of 20 µM BACE1 inhibitor IV (Merck, Calbiochem). Slices were washed for 10 min with HBS pH 5 / 5% BSA three times and further incubated in the buffer for 12 h before mounting with DAPI-containing mounting medium (C. Roth) and sealing with nail polish (essence). Confocal images were taken with the LSM 780 at an optical slice thickness of 3.3 µm (DAPI) or 6.1 µm (**SiR-BACE1**) with the 20x objective and the 405 nm and 633 nm laser lines.

Primary hippocampal neurons were prepared from p2-4 BACE1 wild type and knockout mice as described previously[90] except that 1) tissue was digested without DNase and 2) growth medium was supplemented with 1X pen/strep. At DIV8, cells were stained with 100 nM **SiR-BACE1** in conditioned medium incubated overnight at 37 °C, 5% CO_2. The next day, cells were washed three times with HBS pH 5 and imaged in HBS pH 5.

BACE1 knockout MEF were cultured in fluorodishes (WPI) previously coated with 0.1 mg/mL poly-D-lysine for 20 min. To disrupt lysosomal acidification, cells were treated with 20 nM bafilomycin A1 (BafA1, Sigma-Aldrich) for 4 h. Subsequent double-staining was performed with 75 nM LysotrackerGreen (Thermo Fisher Scientific) and 1 µM **SiR-BACE1** diluted in BafA1-containing conditioned medium for 30 min at 37 °C, 5% CO_2. Cells were

then washed twice with PBS and subjected to confocal imaging in HBS pH 7.4 with the 63x objective and the pinhole set to 1 AU for the SiR channel.

Single molecule tracking

CHO-K1 cells were cultured in TC-treated CellView dishes with glass bottom (Greiner 627860) and transfected with untagged hBACE1 using jetPRIME (Polyplus-transfection). After 1 d, plasma membrane lawns (PML) were generated by incubating the dishes on ice for 5 min, washing twice with ice-cold PBS, incubating on ice in hypotonic 0.3X PML buffer for 5 min, and generating PML by gently pipetting hypotonic 1X PML buffer directly onto the cells.[49] PML were pre-incubated in HBS pH 5 for 5 min at room temperature before being stained with 100 nM **SiR-BACE1** in HBS pH 5 for 2 min on ice. PML were washed three times with and imaged in HBS pH 5.

Time-lapse imaging was performed with a custom-built widefield fluorescence microscope based on an inverse Leica DMi8 equipped with a HC PL APO 63x/1.40 oil immersion objective and supplemented with a 700 mW 640 nm laser diode (Lasertack) coupled into a multimode fiber (Thorlabs), and evolve delta EMCCD camera (Photometics) controlled via Leica Application Suite X software. Laser power at the sample was 8.5 mW. Data were recorded from full camera chip with EM gain 300 at 16-bit with 40 ms interval over 1000 frames.

Time series were imported to Fiji and PML regions were exported as 8-bit gmv files for analysis with the automated single particle tracking (ASPT) algorithm in GMimPro.[91] Full width at half-maximum (FWHM) of diffraction-limited single molecule signals was calculated from the Rayleigh criterion as 292 nm. Velocity was calculated from 5 frames, the maximum search radius for linking signals from frame to frame was 5 pixels, minimum track length was 10 frames, Q threshold (equation 8 in [91]) was 2 (corresponding to a Q value from single particle detection of 0.2), and cluster threshold to exclude bright accumulations from

analysis was 35. Track analysis was performed in Motility[91] except for track intensity distribution, which was fitted to a bi-modal Gaussian curve using Clampfit 10.4 (Molecular Devices).

To demonstrate single molecule character, cells were transfected with 400 ng SNAP-hBACE1 and 600 ng Mls-EGFP. After 1 d of expression, cells were stained with 1 µM SNAP-surface549 (NEB) in RPMI medium, supplemented with 10% FCS and 2 mM L-glutamine, for 50 min at 4 °C. Next, cells were washed 3x with ice-cold medium, subjected to PML generation, washed twice with PBS, and fixed with 4% PFA (see above) / 0.2% glutaraldehyde for 30 min at room temperature. Fixed PML were washed twice with PBS and once with HBS pH 5. For staining, PML were preincubated in HBS pH 5 for 30 min, then incubated with 100 nM **SiR-BACE1** in HBS pH 5 for 2 min at 4 °C, washed twice with HBS pH 5 before being imaged in HBS pH 5. Acquisition was performed at an inverted Zeiss spinning disc microscope equipped with an evolve delta EMCCD camera (Photometics) cooled to -80 °C, a 100 mW 488 nm laser line used at 100%, a 75 mW 561 nm laser line used at 75%, a 75 mW 638 laser line used at 75%, a Plan-Apochromat 63x/1.40 Oil DIC objective, and ZEN 2.0.0.0 blue software with EM gain 300 at 16-bit. For **SiR-BACE1**, 3 consecutive images with an exposure time of 10 s each were acquired, accompanied by single acquisitions of EGFP (1 s exposure) and SNAP (4 s). Stack registration was performed in Fiji with StackReg plugin applying a Rigid Body transformation.

Ancillary Information

Supporting Information

Supplementary Table 1: Analysis data for monoamines SiR-6-CONH-Cn+2-NH2;

Supplementary Table 2: Analysis data for guanidines SiR-6-CONH-Cn+2-NH-C(NH)-NH2;

Supplementary Table 3: Analysis data for inhibitors SiR-6-CONH-Cn+2-Inh.;

Supplementary Figure 1: Purity assessment for 13a-f by analytical HPLC;

Supplementary Figure 2: Conformational change of SiR-BACE1 upon binding to BACE1;

Molecular formula strings

Corresponding Author Information: tobias.huth@fau.de

Author contributions

[§] These authors contributed equally. [§§] These authors share senior authorship.

Acknowledgment

This work was supported by the Deutsche Forschungsgemeinschaft INST 90/675-1 FUGG to C.A., the Staedtler-Stiftung to C.A., the Studienstiftung des deutschen Volkes to S.K. and S.H., and Universitätsbund Erlangen-Nürnberg to S.K. J.B. acknowledges support from the 'EPFL Fellows' fellowship programme co-funded by Marie Skłodowska-Curie, Horizon 2020 Grant agreement no. 665667. K.J. is grateful to funding from the Swiss Science Foundation, the NCCR Chemical Biology and EPFL. We thank Jana Wrosch (Department of Psychiatry and Psychotherapy, Friedrich-Alexander-University (FAU)) and Tobias Kleinhenz (Leica Microsystems, Germany) for supporting the assembly of the single molecule imaging setup; the Core Unit Cell Sorting und Immunomonitoring (FAU) for flow cytometry introduction; Jan-Erik Heil (Zeiss, Germany) for FCS support; Doug Johnson (Pfizer, USA) for providing

S-39 and R-39 for control recordings and for valuable discussions; Alina Tabor-Schkade (Department of Chemistry and Pharmacy, FAU) for single molecule discussions; and Iwona Izydorczyk, Annette Kuhn, Birgit Vogler, and Jana Schramm for technical assistance.

The present work was performed in (partial) fulfillment of the requirements for obtaining the degree Dr. rer. nat.

Abbreviations used

Aβ, amyloid β; AD, Alzheimer's disease; APP, amyloid precursor protein; AU, arbitrary units; BACE, β-site APP-cleaving enzyme; BafA1, bafilomycin A1; CA3, cornu ammonis 3; CHO-K1 cells, Chinese hamster ovary K1 cells; C*x*-linker, linker of *x* methylene groups; DIV, day *in vitro*; ECD, extracellular domain; EGFP, enhanced green fluorescent protein; FCC, flash column chromatography; FCS, fluorescence correlation spectroscopy; FRET, fluorescence resonance energy transfer; HBS, HEPES-buffered saline; HEK-293T cells, human embryonic kidney cells 293 with SV40 large T antigen; KCNQ, voltage-gated potassium channel subfamily Q; K_V, voltage-gated potassium channel; LSM, laser scanning microscope; MEF, mouse embryonic fibroblasts; Mls, membrane localization signal; MSD, mean square displacement; Na_V, voltage-gated sodium channel; PML, plasma membrane lawn; p*x*, postnatal day *x*; ROI, region of interest; RP-HPLC, reversed phase HPLC; SE, standard error; SEM, standard error of the mean; SiR647, silicone rhodamine 647; STED, stimulated emission depletion; TIRF, total internal reflection fluorescence

References

(1) Alzheimer, A. Uber eine eigenartige Erkrankung der Hirnrinde. *Allg Zeitschr f Psychiatr. u Psych-Gerichtl Med* **1907**, *64* (64), 146–148.

(2) Brookmeyer, R.; Gray, S.; Kawas, C. Projections of Alzheimer's Disease in the United States and the Public Health Impact of Delaying Disease Onset. *Am. J. Public Health* **1998**, *88* (9), 1337–1342.

(3) Piaceri, I.; Nacmias, B.; Sorbi, S.; Naemias, B. Genetics of Familial and Sporadic Alzheimer's Disease. *Front. Biosci. (Elite Ed).* **2013**, *5* (5), 167–177.

(4) Alzheimer's Association. Alzheimer's Disease Facts and Figures. *Alzheimers. Dement.* **2016**, *12* (4), 459–509.

(5) Vassar, R.; Kuhn, P. H.; Haass, C.; Kennedy, M. E.; Rajendran, L.; Wong, P. C.; Lichtenthaler, S. F. Function, Therapeutic Potential and Cell Biology of BACE Proteases: Current Status and Future Prospects. *J Neurochem* **2014**, *130* (1), 4–28.

(6) Karran, E.; De Strooper, B. The Amyloid Cascade Hypothesis: Are We Poised for Success or Failure? *J. Neurochem.* **2016**, *139*, 237–252.

(7) Hardy, J. A.; Higgins, G. A. Alzheimer's Disease: The Amyloid Cascade Hypothesis. *Science* **1992**, *256* (5054), 184–185.

(8) Herrup, K. The Case for Rejecting the Amyloid Cascade Hypothesis. *Nat. Neurosci.* **2015**, *18* (6), 794–799.

(9) Choi, S. H.; Kim, Y. H.; Hebisch, M.; Sliwinski, C.; Lee, S.; D'Avanzo, C.; Chen, H.; Hooli, B.; Asselin, C.; Muffat, J.; Klee, J. B.; Zhang, C.; Wainger, B. J.; Peitz, M.; Kovacs, D. M.; Woolf, C. J.; Wagner, S. L.; Tanzi, R. E.; Kim, D. Y. A Three-Dimensional Human Neural Cell Culture Model of Alzheimer's Disease. *Nature* **2014**, *515* (7526), 274–278.

(10) Hussain, I.; Powell, D.; Howlett, D. R.; Tew, D. G.; Meek, T. D.; Chapman, C.;

Gloger, I. S.; Murphy, K. E.; Southan, C. D.; Ryan, D. M.; Smith, T. S.; Simmons, D. L.; Walsh, F. S.; Dingwall, C.; Christie, G. Identification of a Novel Aspartic Protease (Asp 2) as Beta-Secretase. *Mol. Cell. Neurosci.* **1999**, *14* (6), 419–427.

(11) Sinha, S.; Anderson, J. P.; Barbour, R.; Basi, G. S.; Caccavello, R.; Davis, D.; Doan, M.; Dovey, H. F.; Frigon, N.; Hong, J.; Jacobson-Croak, K.; Jewett, N.; Keim, P.; Knops, J.; Lieberburg, I.; Power, M.; Tan, H.; Tatsuno, G.; Tung, J.; Schenk, D.; Seubert, P.; Suomensaari, S. M.; Wang, S.; Walker, D.; Zhao, J.; McConlogue, L.; John, V. Purification and Cloning of Amyloid Precursor Protein Beta-Secretase from Human Brain. *Nature* **1999**, *402* (6761), 537–540.

(12) Vassar, R.; Bennett, B. D.; Babu-Khan, S.; Kahn, S.; Mendiaz, E. A.; Denis, P.; Teplow, D. B.; Ross, S.; Amarante, P.; Loeloff, R.; Lui, Y.; Fisher, S.; Fuller, J.; Edenson, S.; Lile, J.; Jarosinski, M. A.; Biere, A. L.; Curran, E.; Burgess, T.; Louis, J. C.; Collins, F.; Treanor, J.; Rogers, G.; Citron, M. Beta-Secretase Cleavage of Alzheimer's Amyloid Precursor Protein by the Transmembrane Aspartic Protease BACE. *Science* **1999**, *286* (5440), 735–741.

(13) Yan, R.; Bienkowski, M. J.; Shuck, M. E.; Miao, H.; Tory, M. C.; Pauley, A. M.; Brashier, J. R.; Stratman, N. C.; Mathews, W. R.; Buhl, A. E.; Carter, D. B.; Tomasselli, A. G.; Parodi, L. A.; Heinrikson, R. L.; Gurney, M. E. Membrane-Anchored Aspartyl Protease with Alzheimer's Disease Beta-Secretase Activity. *Nature* **1999**, *402* (6761), 533–537.

(14) Lin, X.; Koelsch, G.; Wu, S.; Downs, D.; Dashti, A.; Tang, J. Human Aspartic Protease Memapsin 2 Cleaves the Beta-Secretase Site of Beta-Amyloid Precursor Protein. *Proc. Natl. Acad. Sci. U. S. A.* **2000**, *97* (4), 1456–1460.

(15) Kinoshita, A.; Fukumoto, H.; Shah, T.; Whelan, C. M.; Irizarry, M. C.; Hyman, B. T. Demonstration by FRET of BACE Interaction with the Amyloid Precursor Protein at the Cell Surface and in Early Endosomes. *J. Cell Sci.* **2003**, *116* (16), 3339–3346.

(16) Kandalepas, P. C.; Vassar, R. The Normal and Pathologic Roles of the Alzheimer's β-Secretase, BACE1. *Curr. Alzheimer Res.* **2014**, *11* (5), 441.

(17) Yan, R. Physiological Functions of the β-Site Amyloid Precursor Protein Cleaving Enzyme 1 and 2. *Front. Mol. Neurosci.* **2017**, *10*, 97.

(18) Tanzi, R. E.; Bertram, L. Twenty Years of the Alzheimer's Disease Amyloid Hypothesis: A Genetic Perspective. *Cell* **2005**, *120* (4), 545–555.

(19) Jonsson, T.; Atwal, J. K.; Steinberg, S.; Snaedal, J.; Jonsson, P. V; Bjornsson, S.; Stefansson, H.; Sulem, P.; Gudbjartsson, D.; Maloney, J.; Hoyte, K.; Gustafson, A.; Liu, Y.; Lu, Y.; Bhangale, T.; Graham, R. R.; Huttenlocher, J.; Bjornsdottir, G.; Andreassen, O. A.; Jonsson, E. G.; Palotie, A.; Behrens, T. W.; Magnusson, O. T.; Kong, A.; Thorsteinsdottir, U.; Watts, R. J.; Stefansson, K. A Mutation in APP Protects against Alzheimer's Disease and Age-Related Cognitive Decline. *Nature* **2012**, *488* (7409), 96–99.

(20) Maloney, J. A.; Bainbridge, T.; Gustafson, A.; Zhang, S.; Kyauk, R.; Steiner, P.; van der Brug, M.; Liu, Y.; Ernst, J. A.; Watts, R. J.; Atwal, J. K. Molecular Mechanisms of Alzheimer Disease Protection by the A673T Allele of Amyloid Precursor Protein. *J. Biol. Chem.* **2014**, *289* (45), 30990–31000.

(21) Benilova, I.; Gallardo, R.; Ungureanu, A.-A.; Castillo Cano, V.; Snellinx, A.; Ramakers, M.; Bartic, C.; Rousseau, F.; Schymkowitz, J.; De Strooper, B. The Alzheimer Disease Protective Mutation A2T Modulates Kinetic and Thermodynamic Properties of Amyloid-β (Aβ) Aggregation. *J. Biol. Chem.* **2014**, *289* (45), 30977–30989.

(22) Lehnert, S.; Hartmann, S.; Hessler, S.; Adelsberger, H.; Huth, T.; Alzheimer, C. Ion Channel Regulation by Beta-Secretase BACE1 - Enzymatic and Non-Enzymatic Effects beyond Alzheimer's Disease. *Channels* **2016**, *10* (5), 365–378.

(23) Huth, T.; Alzheimer, C. Voltage-Dependent Na+ Channels as Targets of BACE1 -

Implications for Neuronal Firing and beyond. *Curr Alzheimer Res* **2012**, *9* (2), 184–188.

(24) Hitt, B.; Riordan, S. M.; Kukreja, L.; Eimer, W. A.; Rajapaksha, T. W.; Vassar, R. β-Site Amyloid Precursor Protein (APP)-Cleaving Enzyme 1 (BACE1)-Deficient Mice Exhibit a Close Homolog of L1 (CHL1) Loss-of-Function Phenotype Involving Axon Guidance Defects. *J. Biol. Chem.* **2012**, *287* (46), 38408–38425.

(25) Hyman, B. T.; Van Hoesen, G. W.; Damasio, A. R.; Barnes, C. L. Alzheimer's Disease: Cell-Specific Pathology Isolates the Hippocampal Formation. *Science* **1984**, *225* (4667), 1168–1170.

(26) Gowrishankar, S.; Yuan, P.; Wu, Y.; Schrag, M.; Paradise, S.; Grutzendler, J.; De Camilli, P.; Ferguson, S. M. Massive Accumulation of Luminal Protease-Deficient Axonal Lysosomes at Alzheimer's Disease Amyloid Plaques. *Proc. Natl. Acad. Sci. U. S. A.* **2015**, *112* (28), E3699-E3708.

(27) Sadleir, K. R.; Kandalepas, P. C.; Buggia-Prévot, V.; Nicholson, D. A.; Thinakaran, G.; Vassar, R. Presynaptic Dystrophic Neurites Surrounding Amyloid Plaques Are Sites of Microtubule Disruption, BACE1 Elevation, and Increased Aβ Generation in Alzheimer's Disease. *Acta Neuropathol.* **2016**, *132* (2), 235-256.

(28) Bauereiss, A.; Welzel, O.; Jung, J.; Grosse-Holz, S.; Lelental, N.; Lewczuk, P.; Wenzel, E. M.; Kornhuber, J.; Groemer, T. W. Surface Trafficking of APP and BACE in Live Cells. *Traffic* **2015**, *16* (6), 655-675.

(29) Das, U.; Wang, L.; Ganguly, A.; Saikia, J. M.; Wagner, S. L.; Koo, E. H.; Roy, S. Visualizing APP and BACE-1 Approximation in Neurons Yields Insight into the Amyloidogenic Pathway. *Nat. Neurosci.* **2016**, *19* (1), 55–64.

(30) Ohlendorf, D. H.; Lipscomb, J. D.; Weber, P. C. Alzheimer's Disease. Enter a Protease Inhibitor. *Nature* **1988**, *336* (6156), 403–405.

(31) Qian, X.; Hamad, B.; Dias-Lalcaca, G. The Alzheimer Disease Market. *Nat. Rev. Drug*

Discov. **2015**, *14* (10), 675–676.

(32) Barão, S.; Moechars, D.; Lichtenthaler, S. F.; De Strooper, B. BACE1 Physiological Functions May Limit Its Use as Therapeutic Target for Alzheimer's Disease. *Trends Neurosci.* **2016**, *39* (3), 158-169.

(33) Alzforum. Therapeutics database. https://www.alzforum.org/therapeutics (accessed Jan 5, 2018).

(34) Moussa, C. E. H. Beta-Secretase Inhibitors in Phase I and Phase II Clinical Trials for Alzheimer's Disease. *Expert Opin. Investig. Drugs* **2017**, *26* (10), 1131–1136.

(35) Prati, F.; Bottegoni, G.; Bolognesi, M. L.; Cavalli, A. BACE-1 Inhibitors: From Recent Single-Target Molecules to Multitarget Compounds for Alzheimer's Disease. *J. Med. Chem.* **2018**, *61* (3), 619–637.

(36) Malamas, M. S.; Robichaud, A.; Erdei, J.; Quagliato, D.; Solvibile, W.; Zhou, P.; Morris, K.; Turner, J.; Wagner, E.; Fan, K.; Olland, A.; Jacobsen, S.; Reinhart, P.; Riddell, D.; Pangalos, M. Design and Synthesis of Aminohydantoins as Potent and Selective Human β-Secretase (BACE1) Inhibitors with Enhanced Brain Permeability. *Bioorg. Med. Chem. Lett.* **2010**, *20* (22), 6597–6605.

(37) Malamas, M. S.; Barnes, K.; Johnson, M.; Hui, Y.; Zhou, P.; Turner, J.; Hu, Y.; Wagner, E.; Fan, K.; Chopra, R.; Olland, A.; Bard, J.; Pangalos, M.; Reinhart, P.; Robichaud, A. J. Di-Substituted Pyridinyl Aminohydantoins as Potent and Highly Selective Human β-Secretase (BACE1) Inhibitors. *Bioorg. Med. Chem.* **2010**, *18* (2), 630–639.

(38) Oehlrich, D.; Prokopcova, H.; Gijsen, H. J. M. The Evolution of Amidine-Based Brain Penetrant BACE1 Inhibitors. *Bioorg. Med. Chem. Lett.* **2014**, *24* (9), 2033–2045.

(39) Lukinavičius, G.; Umezawa, K.; Olivier, N.; Honigmann, A.; Yang, G.; Plass, T.; Mueller, V.; Reymond, L.; Corrêa, I. R.; Luo, Z.-G.; Schultz, C.; Lemke, E. A.; Heppenstall, P.; Eggeling, C.; Manley, S.; Johnsson, K. A near-Infrared Fluorophore

for Live-Cell Super-Resolution Microscopy of Cellular Proteins. *Nat. Chem.* **2013**, *5* (2), 132–139.

(40) Li, H.; Tatlock, J.; Linton, A.; Gonzalez, J.; Jewell, T.; Patel, L.; Ludlum, S.; Drowns, M.; Rahavendran, S. V; Skor, H.; Hunter, R.; Shi, S. T.; Herlihy, K. J.; Parge, H.; Hickey, M.; Yu, X.; Chau, F.; Nonomiya, J.; Lewis, C. Discovery of (R)-6-Cyclopentyl-6-(2-(2,6-Diethylpyridin-4-Yl)ethyl)-3-((5,7-Dimethyl-[1,2,4]triazolo[1,5-A]pyrimidin-2-Yl)methyl)-4-Hydroxy-5,6-Dihydropyran-2-One (PF-00868554) as a Potent and Orally Available Hepatitis C Virus Polymerase Inhibitor. *J. Med. Chem.* **2009**, *52* (5), 1255–1258.

(41) Ellis, C. R.; Tsai, C.-C.; Lin, F.-Y.; Shen, J. Conformational Dynamics of Cathepsin D and Binding to a Small-Molecule BACE1 Inhibitor. *J. Comput. Chem.* **2017**, *38* (15), 1260-1269.

(42) Ellis, C. R.; Shen, J. PH-Dependent Population Shift Regulates BACE1 Activity and Inhibition. *J. Am. Chem. Soc.* **2015**, *137* (30), 9543–9546.

(43) Shimizu, H.; Tosaki, A.; Kaneko, K.; Hisano, T.; Sakurai, T.; Nukina, N. Crystal Structure of an Active Form of BACE1, an Enzyme Responsible for Amyloid Beta Protein Production. *Mol. Cell. Biol.* **2008**, *28* (11), 3663–3671.

(44) Stachel, S. J.; Coburn, C. A.; Steele, T. G.; Jones, K. G.; Loutzenhiser, E. F.; Gregro, A. R.; Rajapakse, H. A.; Lai, M.-T.; Crouthamel, M.-C.; Xu, M.; Tugusheva, K.; Lineberger, J. E.; Pietrak, B. L.; Espeseth, A. S.; Shi, X.-P.; Chen-Dodson, E.; Holloway, M. K.; Munshi, S.; Simon, A. J.; Kuo, L.; Vacca, J. P. Structure-Based Design of Potent and Selective Cell-Permeable Inhibitors of Human β-Secretase (BACE-1). *J. Med. Chem.* **2004**, *47* (26), 6447–6450.

(45) Laird, F. M.; Cai, H.; Savonenko, A. V; Farah, M. H.; He, K.; Melnikova, T.; Wen, H.; Chiang, H.-C.; Xu, G.; Koliatsos, V. E.; Borchelt, D. R.; Price, D. L.; Lee, H.-K.; Wong, P. C. BACE1, a Major Determinant of Selective Vulnerability of the Brain to

Amyloid-Beta Amyloidogenesis, Is Essential for Cognitive, Emotional, and Synaptic Functions. *J. Neurosci.* **2005**, *25* (50), 11693–11709.

(46) Kandalepas, P. C.; Sadleir, K. R.; Eimer, W. A.; Zhao, J.; Nicholson, D. A.; Vassar, R. The Alzheimer's β-Secretase BACE1 Localizes to Normal Presynaptic Terminals and to Dystrophic Presynaptic Terminals Surrounding Amyloid Plaques. *Acta Neuropathol.* **2013**, *126* (3), 329–352.

(47) Agostinho, P.; Pliássova, A.; Oliveira, C. R.; Cunha, R. A. Localization and Trafficking of Amyloid-β Protein Precursor and Secretases: Impact on Alzheimer's Disease. *J. Alzheimers. Dis.* **2015**, *45* (2), 329-347.

(48) Jiang, S.; Li, Y.; Zhang, X.; Bu, G.; Xu, H.; Zhang, Y. W. Trafficking Regulation of Proteins in Alzheimer's Disease. *Mol Neurodegener* **2014**, *9* (1), 6.

(49) Moreno, C.; Oliveras, A.; de la Cruz, A.; Bartolucci, C.; Muñoz, C.; Salar, E.; Gimeno, J. R.; Severi, S.; Comes, N.; Felipe, A.; González, T.; Lambiase, P.; Valenzuela, C. A New KCNQ1 Mutation at the S5 Segment That Impairs Its Association with KCNE1 Is Responsible for Short QT Syndrome. *Cardiovasc. Res.* **2015**, *107* (4), 613-623.

(50) Mashanov, G. I.; Nobles, M.; Harmer, S. C.; Molloy, J. E.; Tinker, A. Direct Observation of Individual KCNQ1 Potassium Channels Reveals Their Distinctive Diffusive Behavior. *J Biol Chem* **2010**, *285* (6), 3664–3675.

(51) Casey, J. R.; Grinstein, S.; Orlowski, J. Sensors and Regulators of Intracellular pH. *Nat. Rev. Mol. Cell Biol.* **2010**, *11* (1), 50–61.

(52) Harris, R. C., Tsai, C.-C., Ellis, C. R., Shen, J. Proton-Coupled Conformational Allostery Modulates the Inhibitor Selectivity for β-Secretase. *J. Phys. Chem. Lett.* **2017**, *8* (19), 4832–4837.

(53) Ellis, C. R., Tsai, C.-C., Hou, X., Shen, J. Constant pH Molecular Dynamics Reveals pH-Modulated Binding of Two Small-Molecule BACE1 Inhibitors. *J. Phys. Chem. Lett.* **2016**, *7*(6), 944–949.

(54) Lukinavičius, G.; Blaukopf, C.; Pershagen, E.; Schena, A.; Reymond, L.; Derivery, E.; Gonzalez-Gaitan, M.; D'Este, E.; Hell, S. W.; Gerlich, D. W.; Johnsson, K. SiR-Hoechst Is a Far-Red DNA Stain for Live-Cell Nanoscopy. *Nat. Commun.* **2015**, 6, 8497.

(55) Zuhl, A. M.; Nolan, C. E.; Brodney, M. A.; Niessen, S.; Atchison, K.; Houle, C.; Karanian, D. A.; Ambroise, C.; Brulet, J. W.; Beck, E. M.; Doran, S. D.; O'Neill, B. T.; am Ende, C. W.; Chang, C.; Geoghegan, K. F.; West, G. M.; Judkins, J. C.; Hou, X.; Riddell, D. R.; Johnson, D. S. Chemoproteomic Profiling Reveals That Cathepsin D off-Target Activity Drives Ocular Toxicity of β-Secretase Inhibitors. *Nat. Commun.* **2016**, *7*, 13042.

(56) Liebsch, F.; Aurousseau, M. R. P.; Bethge, T.; McGuire, H.; Scolari, S.; Herrmann, A.; Blunck, R.; Bowie, D.; Multhaup, G. Full-Length Cellular Beta-Secretase Has a Trimeric Subunit Stoichiometry, and Its Sulfur-Rich Transmembrane Interaction Site Modulates Cytosolic Copper Compartmentalization. *J. Biol. Chem.* **2017**, *292* (32), 13258-13270.

(57) Sahl, S. J.; Hell, S. W.; Jakobs, S. Fluorescence Nanoscopy in Cell Biology. *Nat. Rev. Mol. Cell Biol.* **2017**, *18* (11), 685–701.

(58) Weisenburger, S.; Boening, D.; Schomburg, B.; Giller, K.; Becker, S.; Griesinger, C.; Sandoghdar, V. Cryogenic Optical Localization Provides 3D Protein Structure Data with Angstrom Resolution. *Nat. Methods* **2017**, *14* (2), 141–144.

(59) Ulbrich, M. H.; Isacoff, E. Y. Subunit Counting in Membrane-Bound Proteins. *Nat Methods* **2007**, *4* (4), 319–321.

(60) McGuire, H.; Aurousseau, M. R.; Bowie, D.; Blunck, R. Automating Single Subunit Counting of Membrane Proteins in Mammalian Cells. *J Biol Chem* **2012**, *287* (43), 35912–35921.

(61) Biermann, B.; Sokoll, S.; Klueva, J.; Missler, M.; Wiegert, J. S.; Sibarita, J. B.; Heine,

M. Imaging of Molecular Surface Dynamics in Brain Slices Using Single-Particle Tracking. *Nat Commun* **2014**, *5*, 3024.

(62) Calebiro, D.; Rieken, F.; Wagner, J.; Sungkaworn, T.; Zabel, U.; Borzi, A.; Cocucci, E.; Zurn, A.; Lohse, M. J. Single-Molecule Analysis of Fluorescently Labeled G-Protein-Coupled Receptors Reveals Complexes with Distinct Dynamics and Organization. *Proc Natl Acad Sci U S A* **2013**, *110* (2), 743–748.

(63) Tabor, A.; Weisenburger, S.; Banerjee, A.; Purkayastha, N.; Kaindl, J. M.; Hübner, H.; Wei, L.; Grömer, T. W.; Kornhuber, J.; Tschammer, N.; Birdsall, N. J. M.; Mashanov, G. I.; Sandoghdar, V.; Gmeiner, P. Visualization and Ligand-Induced Modulation of Dopamine Receptor Dimerization at the Single Molecule Level. *Sci. Rep.* **2016**, *6*, 33233.

(64) Dorsch, S.; Klotz, K.-N.; Engelhardt, S.; Lohse, M. J.; Bünemann, M. Analysis of Receptor Oligomerization by FRAP Microscopy. *Nat. Methods* **2009**, *6* (3), 225–230.

(65) Pantoja, R.; Rodriguez, E. A.; Dibas, M. I.; Dougherty, D. A.; Lester, H. A. Single-Molecule Imaging of a Fluorescent Unnatural Amino Acid Incorporated into Nicotinic Receptors. *Biophys J* **2009**, *96* (1), 226–237.

(66) Ortega-Arroyo, J.; Kukura, P. Interferometric Scattering Microscopy (iSCAT): New Frontiers in Ultrafast and Ultrasensitive Optical Microscopy. *Phys. Chem. Chem. Phys.* **2012**, *14* (45), 15625.

(67) McDonald, M.; Gemeinhardt, A.; König, K.; Piliarik, M.; Schaffer, S.; Völkl, S.; Aigner, M.; Mackensen, A.; Sandoghdar, V. Visualizing Single-Cell Secretion Dynamics with Single Protein Sensitivity. *Nano Lett.* **2018**, *18* (1), 513-519.

(68) Nenasheva, T. A.; Neary, M.; Mashanov, G. I.; Birdsall, N. J.; Breckenridge, R. A.; Molloy, J. E. Abundance, Distribution, Mobility and Oligomeric State of M□ Muscarinic Acetylcholine Receptors in Live Cardiac Muscle. *J Mol Cell Cardiol* **2013**, *57* (1), 129–136.

(69) Weron, A.; Burnecki, K.; Akin, E. J.; Solé, L.; Balcerek, M.; Tamkun, M. M.; Krapf, D. Ergodicity Breaking on the Neuronal Surface Emerges from Random Switching between Diffusive States. *Sci. Rep.* **2017**, *7* (1), 5404.

(70) Massignan, P.; Manzo, C.; Torreno-Pina, J. A.; García-Parajo, M. F.; Lewenstein, M.; Lapeyre, G. J. Nonergodic Subdiffusion from Brownian Motion in an Inhomogeneous Medium. *Phys. Rev. Lett.* **2014**, *112* (15), 150603.

(71) Kusumi, A.; Nakada, C.; Ritchie, K.; Murase, K.; Suzuki, K.; Murakoshi, H.; Kasai, R. S.; Kondo, J.; Fujiwara, T. Paradigm Shift of the Plasma Membrane Concept from the Two-Dimensional Continuum Fluid to the Partitioned Fluid: High-Speed Single-Molecule Tracking of Membrane Molecules. *Annu. Rev. Biophys. Biomol. Struct.* **2005**, *34* (1), 351–378.

(72) Eggeling, C.; Ringemann, C.; Medda, R.; Schwarzmann, G.; Sandhoff, K.; Polyakova, S.; Belov, V. N.; Hein, B.; von Middendorff, C.; Schönle, A.; Hell, S. W. Direct Observation of the Nanoscale Dynamics of Membrane Lipids in a Living Cell. *Nature* **2009**, *457* (7233), 1159–1162.

(73) Lingwood, D.; Simons, K. Lipid Rafts As a Membrane-Organizing Principle. *Science* **2010**, *327* (5961), 46–50.

(74) Huth, T.; Schmidt-Neuenfeldt, K.; Rittger, A.; Saftig, P.; Reiss, K.; Alzheimer, C. Non-Proteolytic Effect of Beta-Site APP-Cleaving Enzyme 1 (BACE1) on Sodium Channel Function. *Neurobiol Dis* **2009**, *33* (2), 282–289.

(75) Agsten, M.; Hessler, S.; Lehnert, S.; Volk, T.; Rittger, A.; Hartmann, S.; Raab, C.; Kim, D. Y.; Groemer, T. W.; Schwake, M.; Alzheimer, C.; Huth, T. BACE1 Modulates Gating of KCNQ1 (Kv7.1) and Cardiac Delayed Rectifier KCNQ1/KCNE1 (IKs). *J. Mol. Cell. Cardiol.* **2015**, *89* (Pt B), 335–348.

(76) Hessler, S.; Zheng, F.; Hartmann, S.; Rittger, A.; Lehnert, S.; Volkel, M.; Nissen, M.; Edelmann, E.; Saftig, P.; Schwake, M.; Huth, T.; Alzheimer, C. Beta-Secretase BACE1

Regulates Hippocampal and Reconstituted M-Currents in a Beta-Subunit-Like Fashion. *J. Neurosci.* **2015**, *35* (8), 3298–3311.

(77) Hartmann, S.; Zheng, F.; Kyncl, M. C.; Karch, S.; Voelkl, K.; Zott, B.; D'Avanzo, C.; Lomoio, S.; Tesco, G.; Kim, D. Y.; Alzheimer, C.; Huth, T. β-Secretase BACE1 Promotes Surface Expression and Function of Kv3.4 at Hippocampal Mossy Fiber Synapses. *J. Neurosci.* **2018**, *38* (14), 3480-3494.

(78) Pan, Z.; Kao, T.; Horvath, Z.; Lemos, J.; Sul, J.-Y.; Cranstoun, S. D.; Bennett, V.; Scherer, S. S.; Cooper, E. C. A Common Ankyrin-G-Based Mechanism Retains KCNQ and NaV Channels at Electrically Active Domains of the Axon. *J. Neurosci.* **2006**, *26* (10), 2599–2613.

(79) Marx, S. O.; Kurokawa, J.; Reiken, S.; Motoike, H.; D'Armiento, J.; Marks, A. R.; Kass, R. S. Requirement of a Macromolecular Signaling Complex for Beta Adrenergic Receptor Modulation of the KCNQ1-KCNE1 Potassium Channel. *Science* **2002**, *295* (5554), 496–499.

(80) Zhu, D.; Bungart, B. L.; Yang, X.; Zhumadilov, Z.; Lee, J. C.-M.; Askarova, S. Role of Membrane Biophysics in Alzheimer's-related Cell Pathways. *Front. Neurosci.* **2015**, *9*, 186.

(81) Cossec, J.-C.; Simon, A.; Marquer, C.; Moldrich, R. X.; Leterrier, C.; Rossier, J.; Duyckaerts, C.; Lenkei, Z.; Potier, M.-C. Clathrin-Dependent APP Endocytosis and Aβ Secretion Are Highly Sensitive to the Level of Plasma Membrane Cholesterol. *Biochim. Biophys. Acta - Mol. Cell Biol. Lipids* **2010**, *1801* (8), 846–852.

(82) Marquer, C.; Devauges, V.; Cossec, J.-C.; Liot, G.; Lecart, S.; Saudou, F.; Duyckaerts, C.; Leveque-Fort, S.; Potier, M.-C. Local Cholesterol Increase Triggers Amyloid Precursor Protein-Bace1 Clustering in Lipid Rafts and Rapid Endocytosis. *FASEB J.* **2011**, *25* (4), 1295–1305.

(83) Wong, H. S.; Jaumouille, V.; Heit, B.; Doodnauth, S. A.; Patel, S.; Huang, Y.-W.;

Grinstein, S.; Robinson, L. A. Cytoskeletal Confinement of CX3CL1 Limits Its Susceptibility to Proteolytic Cleavage by ADAM10. *Mol. Biol. Cell* **2014**, *25* (24), 3884–3899.

(84) Rajendran, L.; Schneider, A.; Schlechtingen, G.; Weidlich, S.; Ries, J.; Braxmeier, T.; Schwille, P.; Schulz, J. B.; Schroeder, C.; Simons, M.; Jennings, G.; Knolker, H. J.; Simons, K. Efficient Inhibition of the Alzheimer's Disease Beta-Secretase by Membrane Targeting. *Science* **2008**, *320* (5875), 520–523.

(85) Ben Halima, S.; Mishra, S.; Raja, K. M. P.; Willem, M.; Baici, A.; Simons, K.; Brüstle, O.; Koch, P.; Haass, C.; Caflisch, A.; Rajendran, L. Specific Inhibition of β-Secretase Processing of the Alzheimer Disease Amyloid Precursor Protein. *Cell Rep.* **2016**, *14* (9), 2127-2141.

(86) Kalay, Z.; Fujiwara, T. K.; Kusumi, A. Confining Domains Lead to Reaction Bursts: Reaction Kinetics in the Plasma Membrane. *PLoS One* **2012**, *7* (3), e32948.

(87) Dominguez, D.; Tournoy, J.; Hartmann, D.; Huth, T.; Cryns, K.; Deforce, S.; Serneels, L.; Camacho, I. E.; Marjaux, E.; Craessaerts, K.; Roebroek, A. J.; Schwake, M.; D'Hooge, R.; Bach, P.; Kalinke, U.; Moechars, D.; Alzheimer, C.; Reiss, K.; Saftig, P.; De Strooper, B. Phenotypic and Biochemical Analyses of BACE1- and BACE2-Deficient Mice. *J Biol Chem* **2005**, *280* (35), 30797–30806.

(88) McCabe, J. B.; Berthiaume, L. G. Functional Roles for Fatty Acylated Amino-Terminal Domains in Subcellular Localization. *Mol. Biol. Cell* **1999**, *10* (11), 3771–3786.

(89) Schindelin, J.; Arganda-Carreras, I.; Frise, E.; Kaynig, V.; Longair, M.; Pietzsch, T.; Preibisch, S.; Rueden, C.; Saalfeld, S.; Schmid, B.; Tinevez, J. Y.; White, D. J.; Hartenstein, V.; Eliceiri, K.; Tomancak, P.; Cardona, A. Fiji: An Open-Source Platform for Biological-Image Analysis. *Nat Methods* **2012**, *9* (7), 676–682.

(90) Welzel, O.; Tischbirek, C. H.; Jung, J.; Kohler, E. M.; Svetlitchny, A.; Henkel, A. W.; Kornhuber, J.; Groemer, T. W. Synapse Clusters Are Preferentially Formed by

Synapses with Large Recycling Pool Sizes. *PLoS One* **2010**, *5* (10), e13514.

(91) Mashanov, G. I.; Molloy, J. E. Automatic Detection of Single Fluorophores in Live Cells. *Biophys J* **2007**, *92* (6), 2199–2211.

Figures

Figure 1. SiR-BACE1 was developed as a novel fluorogenic BACE1 probe.

A, Development of the new small molecule BACE1 probe SiR-BACE1, which is present in its dark state in solution and shows its fluorogenicity upon binding to BACE1. **B**, SiR-BACE1 was designed as a dyadic conjugate of the small molecule BACE1 inhibitor S-39 and the far-red fluorogenic dye SiR647 with a variable linker of 2 (C2, n = 0), 3, 4, 5, 6, or 8 (C8, n = 6) methylene spacers. Synthesis was performed as shown in **C** with late-stage linker introduction that allows efficient diversification. **D**, Normalized absorption and emission spectra were recorded from the conjugate with a 4-carbon linker (SiR-BACE1) in PBS with 0.2% SDS. **E**, Fluorogenicity of SiR647 was preserved as shown by the absorption of SiR-BACE1 in PBS *versus* PBS with 0.2% SDS. Absorption spectra are depicted as a 10-point average (D,E). **F**, Fluorogenic on-switch could also be induced by incubation of SiR-BACE1 with 200 nM recombinant BACE1 protein in HBS pH 5.

Figure 2. Optimized linker length ensures specific BACE1 staining and inhibition.

A-B, HEK293T cells were transiently transfected with BACE1-EGFP and stained with 100 nM of the conjugates with different linker lengths (C2-6, C8) in pH 5. Representative images from 3 independent experiments are depicted (**A**). Scale bars: 20 µm. **B,** Color-coded colocalization plots of EGFP and SiR647 pixel intensities show the fluorophores' colocalization for the merged images shown in A (whole frame), and for representative regions of interest covering the plasma membrane (membrane ROI) or an intracellular cluster (cluster ROI). **C-D,** Inhibition of BACE1 enzymatic activity by the conjugates was tested with a FRET-based enzymatic assay (inset), in which a substrate holds a donor fluorophore (D) that is quenched by an acceptor (A) until BACE1 cleaves the molecule to release the donor fluorophore. Intensity of the dequenched product is displayed as mean ± SEM for different

concentrations of SiR-BACE1, superimposed with a logistic fit (**C**). IC_{50} for all conjugates was determined from respective logistic data fits (mean ± SE) and analyzed by k-means cluster analysis (**D**). *** $p < 0.001$ (ANOVA).

Figure 3. Fluorogenic switch is promoted in pH 5.

A-F, 100 nM SiR-BACE1 were incubated with different concentrations of recombinant BACE1 extracellular domain. Diffusion of SiR-BACE1 was analyzed by fluorescence correlation spectroscopy (FCS). **A** shows representative raw data (grey) with their fit (black) in the absence of BACE1 in pH 5. **B-C**, Changes in SiR-BACE1 diffusion upon adding 2µM BACE1 protein were followed by time-lapse FCS. **B**, With BACE1, a second fraction with slower diffusion increases over time. Grey dots represent data from 3 independent experiments fitted to an exponential curve (black line). The diffusion time of this slow fraction is stable over time (**C**), indicated by a linear horizontal fit (black line) of the data (grey dots). **D-F,** End-point FCS was recorded with different BACE1 concentrations. **D**, Representative normalized raw data demonstrate a shift towards longer diffusion times with increasing BACE1 concentrations, which indicates decelerated diffusion due to complex formation with BACE1. The fraction of slowly diffusing SiR-BACE1, indicating SiR-BACE1-BACE1 complexes (**E**), and the count rate (CR), indicating fluorescent SiR-BACE1 concentration (**F**), were plotted as a function of BACE1 concentration. Data was collected in pH 5 (black) and pH 7.4 (green) in 3 independent experiments (dots) and fitted to logistic curves (lines). * $p < 0.05$ (2-sample t-test). **G-H,** pH dependency of staining in cellular environment was evaluated on HEK293T cells transiently expressing BACE1-EGFP. **G**, SiR-BACE1 patterns were compared for staining living cells with 100 nM SiR-BACE1 in pH 5 or pH 7.4. Scale bars: 10 µm. **H,** Cells were fixed and stained with 100 nM SiR-BACE1 in pH 7.4 for 10 min at 4 °C. Fluorescence was monitored over 2 h with an interval of 3 min. Medium was changed from HBS pH 7.4 to HBS pH 5 after 60 min. Representative images are

shown at the end of the incubation periods at pH 7.4 and pH 5. Scale bar: 20 µm. **I**, pH dependency of BACE1 inhibition by SiR-BACE1 was assessed with a FRET-based enzymatic assay in HBS pH 5, 7.4, or 8, which affected BACE1 activity (upper panel), but not inhibition (lower panel). Data is given as mean ± SE.

Figure 4. SiR-BACE1 binds to BACE1 with high affinity and specificity in cellular environment.

A-C, HEK293T cells were transiently transfected with BACE1-EGFP and stained with different concentrations of SiR-BACE1. 35,000 cells per condition were analyzed by flow cytometry. n = 3. **A**, Correlation between cells' EGFP and SiR-BACE1 intensities (AU) is depicted for three exemplary SiR-BACE1 concentrations from one representative recording series. Data were fitted to a bilinear custom function (thick lines). The slope of the second component indicated specific SiR-BACE1 staining, summarized as mean ± SEM and superimposed with a logistic fit (red) in **B**. **C**, In order to test for target specificity, cells were stained with 70 nM SiR-BACE1 in the presence of different concentrations of the BACE1 inhibitor IV, which competed with SiR-BACE1 for BACE1 binding. IC_{50} was determined by a logistic fit (red). **D**, HEK293T cells were transiently transfected with EGFP fusion constructs of BACE1, BACE1(D289N), BACE2, or cathepsin-D and stained with 100 nM SiR-BACE1. Scale bars: 10 µm.

Figure 5. SiR-BACE1 marks BACE1 for super-resolution imaging by stimulated emission depletion (STED) microscopy.

A, N1E-115 neuroblastoma cells were transiently transfected with BACE1-EGFP and stained with SiR-BACE1. A confocal image was recorded with LSM780. Scale bar: 30 µm. **B,** A neurite was imaged with the STED setup in confocal mode and is shown as EGFP/SiR-

BACE1 merge. Scale bar: 10 μm. The boxed detail is depicted as confocal and corresponding STED image in **C**. Scale bar: 1 μm. Profile lines were drawn over corresponding structures in STED and confocal image and intensities were plotted for representative cross profile (green box and curve) or neighbouring vesicular structures (red box and curve) from STED image or the corresponding structures in the confocal image (grey curves).

Figure 6. SiR-BACE1 visualizes endogenous BACE1 in fixed neuronal tissue.

A-B, Endogenous BACE1 was visualized by SiR-BACE1 in native hippocampal brain slices from BACE1 wild type (WT) or knockout (KO) mice. **A,** WT and KO slices were stained with 1 μM SiR-BACE1 and depicted as merged (upper panel) or single channel images (lower panel). **B**, Target-specific staining in WT was evaluated by competition with the unlabeled BACE1 inhibitor IV. A-B, Scale bar: 300 μm. **C**, In living primary hippocampal neurons from BACE1 WT or KO mice, SiR-BACE1 incubation resulted in unspecific staining. Note that the SiR channel is overexposed to emphasize the intense accumulations. Scale bars: 50 μm. **D**, Unspecific staining was further analyzed in living BACE1 knockout mouse embryonic fibroblasts (MEF). SiR-BACE1 puncta co-localized with LysoTracker Green (upper panel, DMSO control) and both SiR-BACE1 and lysosomal marker staining were abolished by pretreatment with 20 nM bafilomycin A1 (BafA1) for 4 h. Scale bar: 10 μm.

Figure 7. SiR-BACE1-mediated single particle tracking of BACE1 demonstrates restricted diffusion in the plasma membrane.

A-H, BACE1 diffusion was monitored in plasma membrane lawns (PML) from CHO-K1 cells transiently transfected with untagged BACE1 and stained with 100 nM SiR-BACE1. **A**, Control images of transfected or untransfected PML with or without SiR-BACE1 staining validated specificity. Scale bar: 5 μm. **B,** SiR-BACE1 signals in the probe (A, right panel)

were followed over 1,000 frames with an interval of 40 ms. Individual tracks are depicted in random color. **C,** Distribution of the tracks' intensities (grey bars) was fitted to a bi-modal Gaussian curve (black component and red bi-modal graphs). **D**, Velocity of BACE1 (black dots) was independent from track intensity (red curve, reproduced from C). **E** depicts track lifetime (grey line, reproduced in F), which showed no influence on BACE1 mobility (**F**, black dots). **G**, Mean square displacement (MSD, black squares) over time demonstrates confined movement of BACE1. **H** shows the distribution of individual SiR-BACE1 signals' mobility. Data is given as mean ± SE (D,F,G). n= 418 tracks (B) or 1429 tracks (C-H). **I-J**, Single molecule character of SiR-BACE1 signals was confirmed by following their intensity in fixed PML expressing membrane-targeted EGFP (**I**, green) and SNAP-hBACE1, which was stained with SNAP-surface549 (orange, overexposed) and SiR-BACE1 (greyscale). Scale bar: 3 μm. **J**, Single-step bleaching between frames confirmed presence of single SiR-BACE1 molecules (colored arrows). Scale bar: 4 μm.

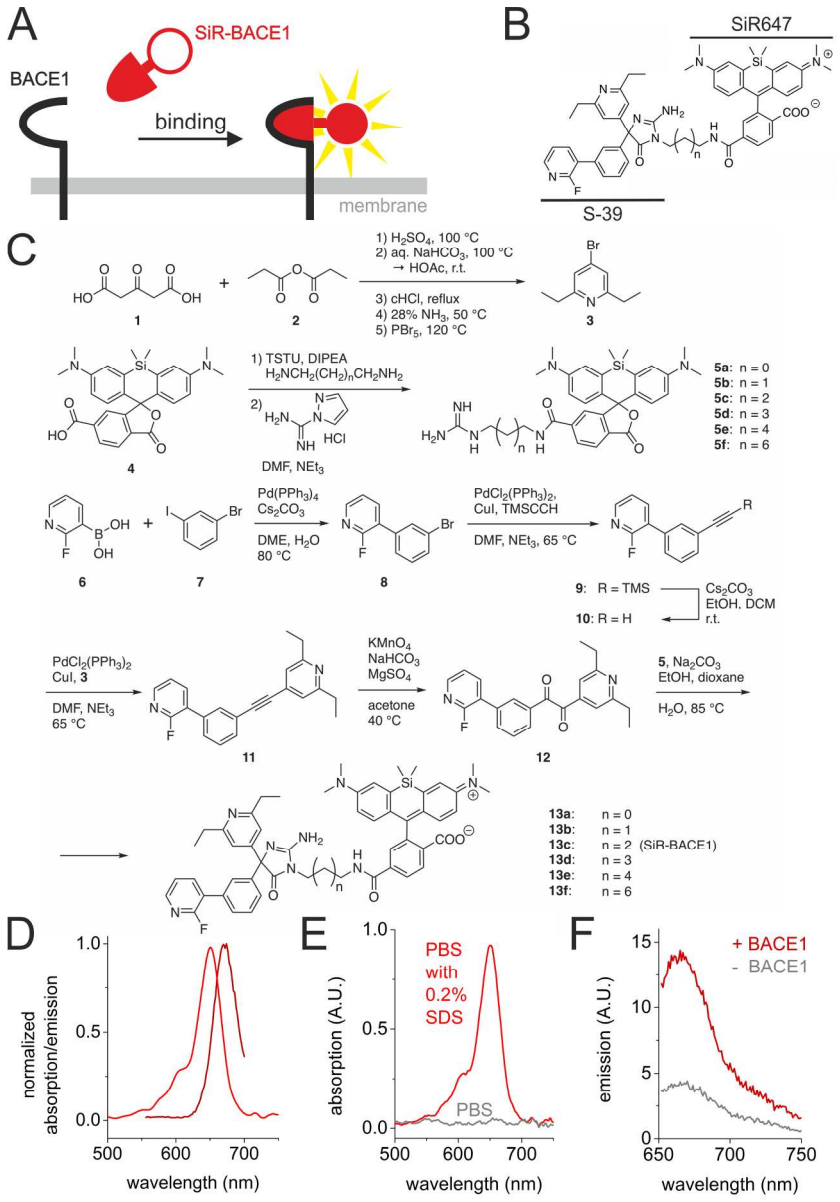

Figure 1

158x229mm (300 x 300 DPI)

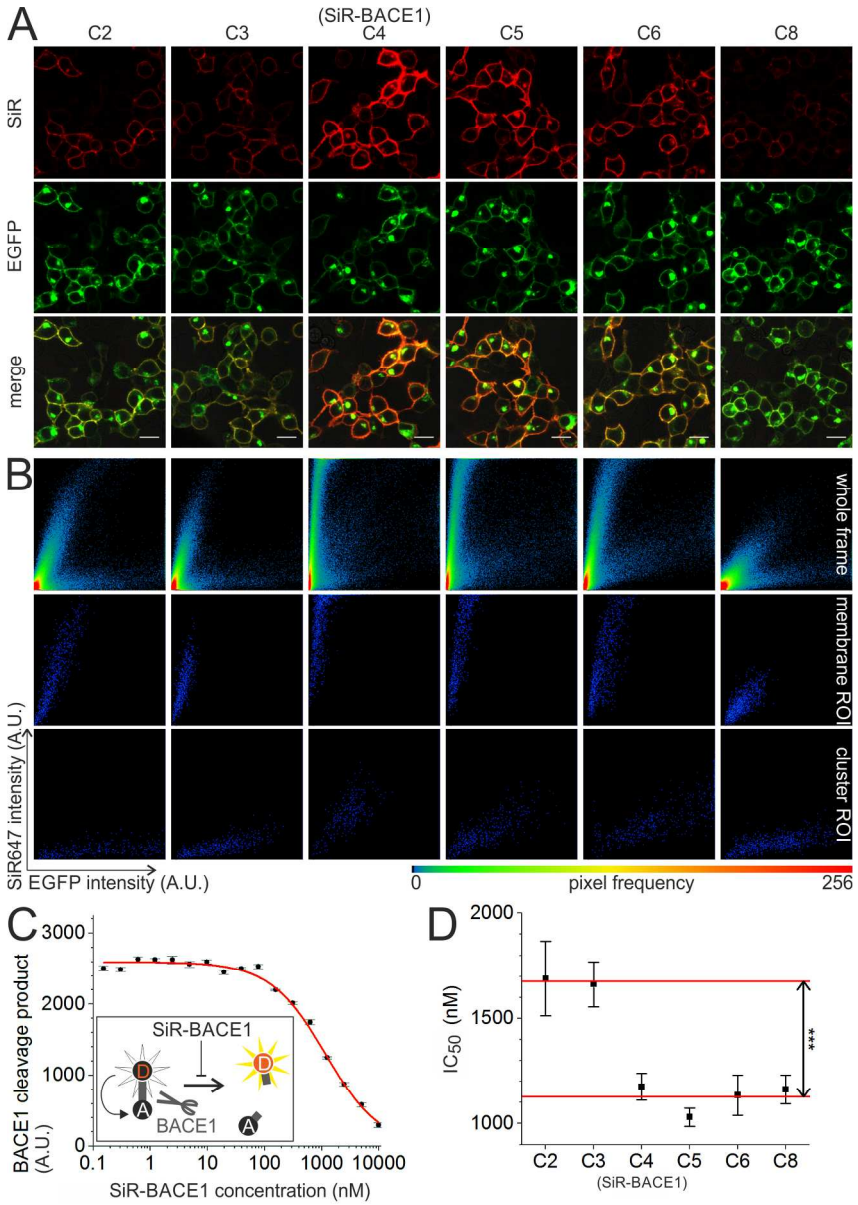

Figure 2

160x227mm (300 x 300 DPI)

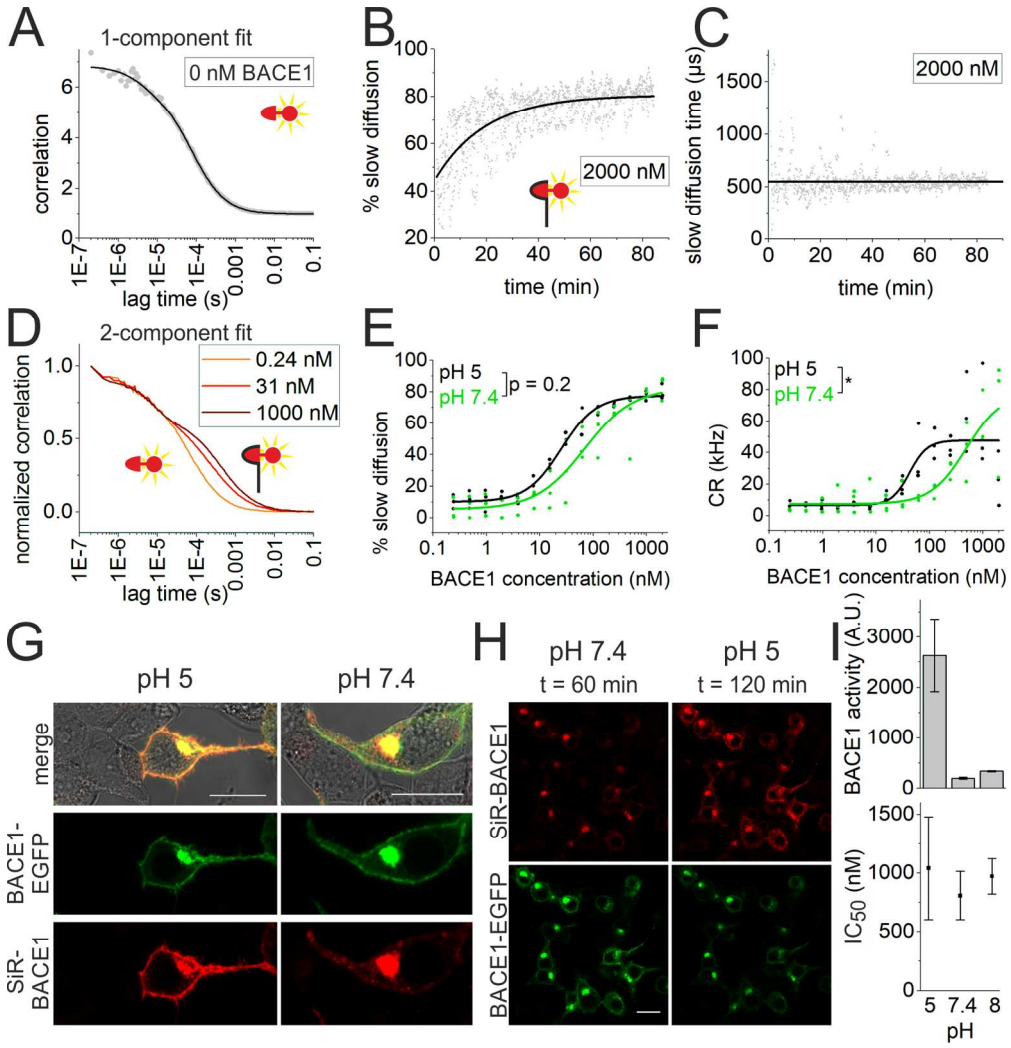

Figure 3

160x165mm (300 x 300 DPI)

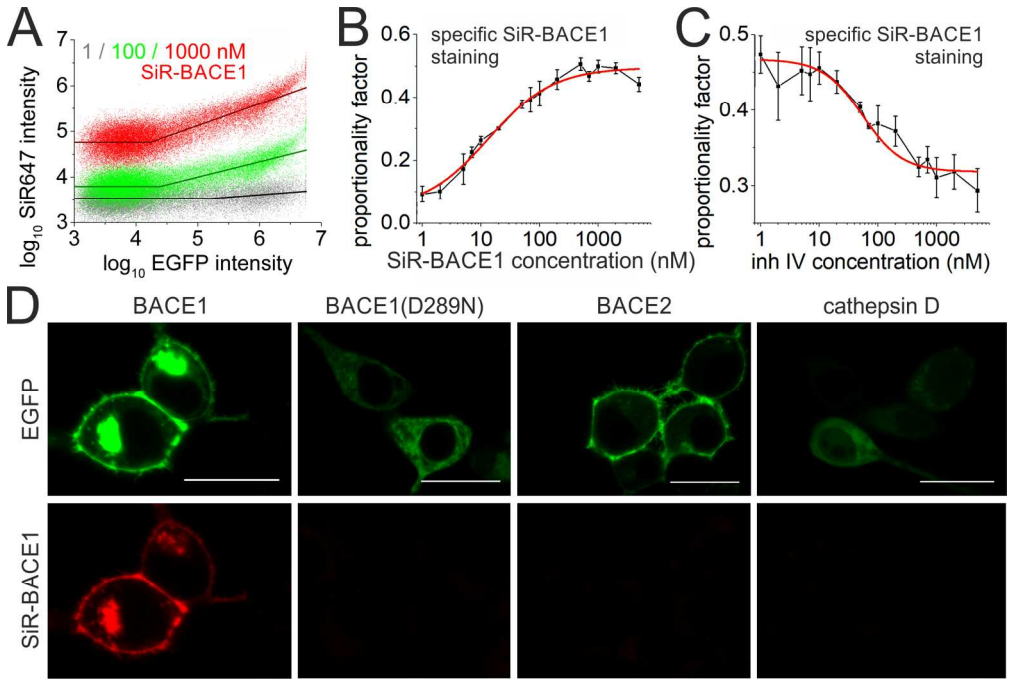

Figure 4

160x107mm (300 x 300 DPI)

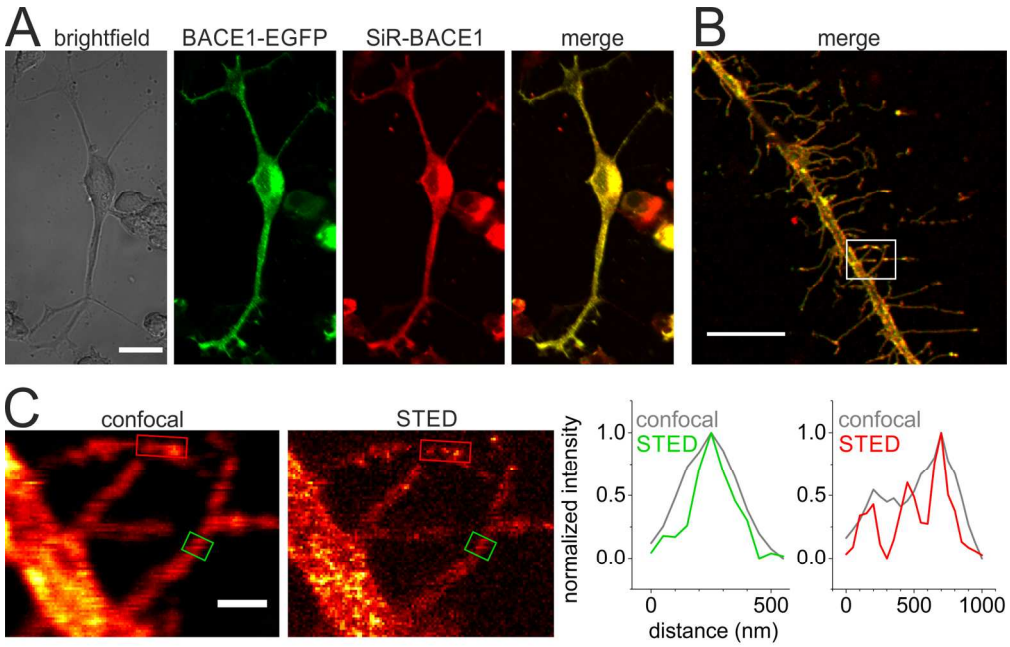

Figure 5

160x103mm (300 x 300 DPI)

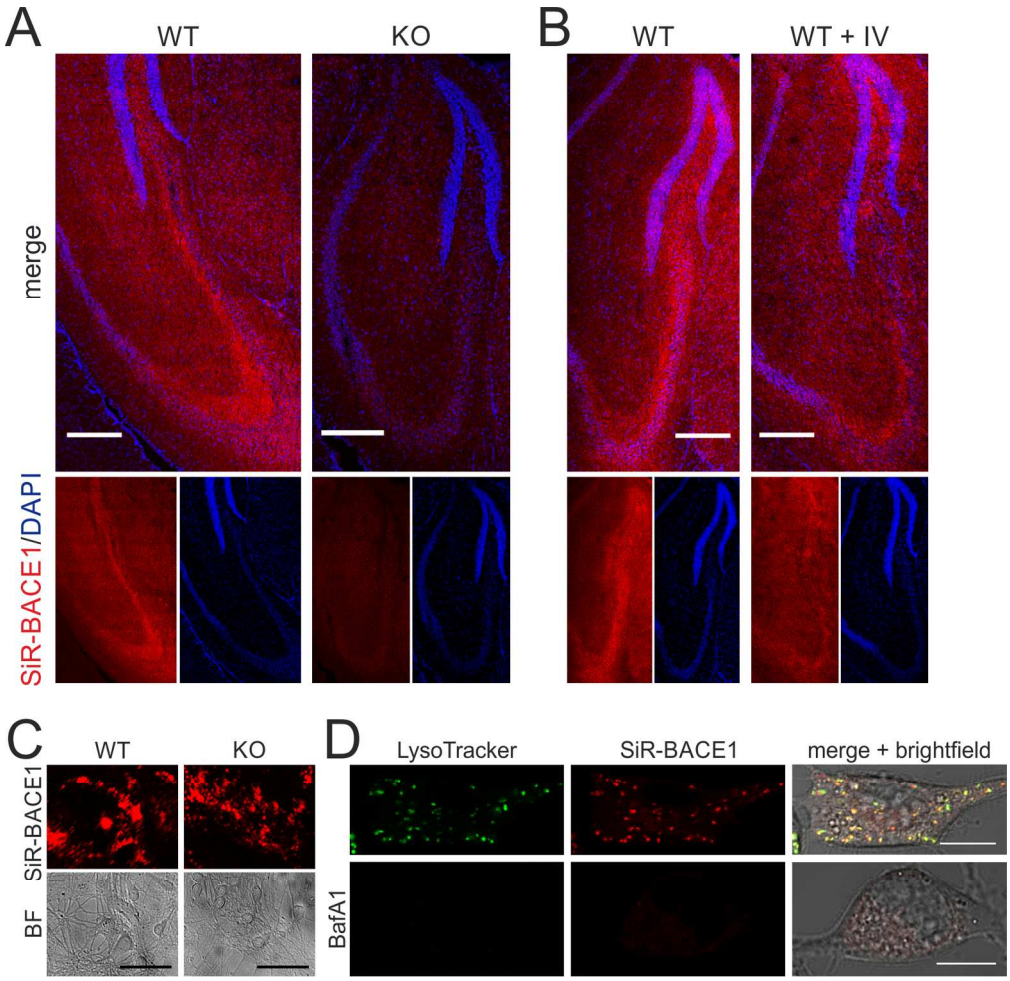

Figure 6

160x155mm (300 x 300 DPI)

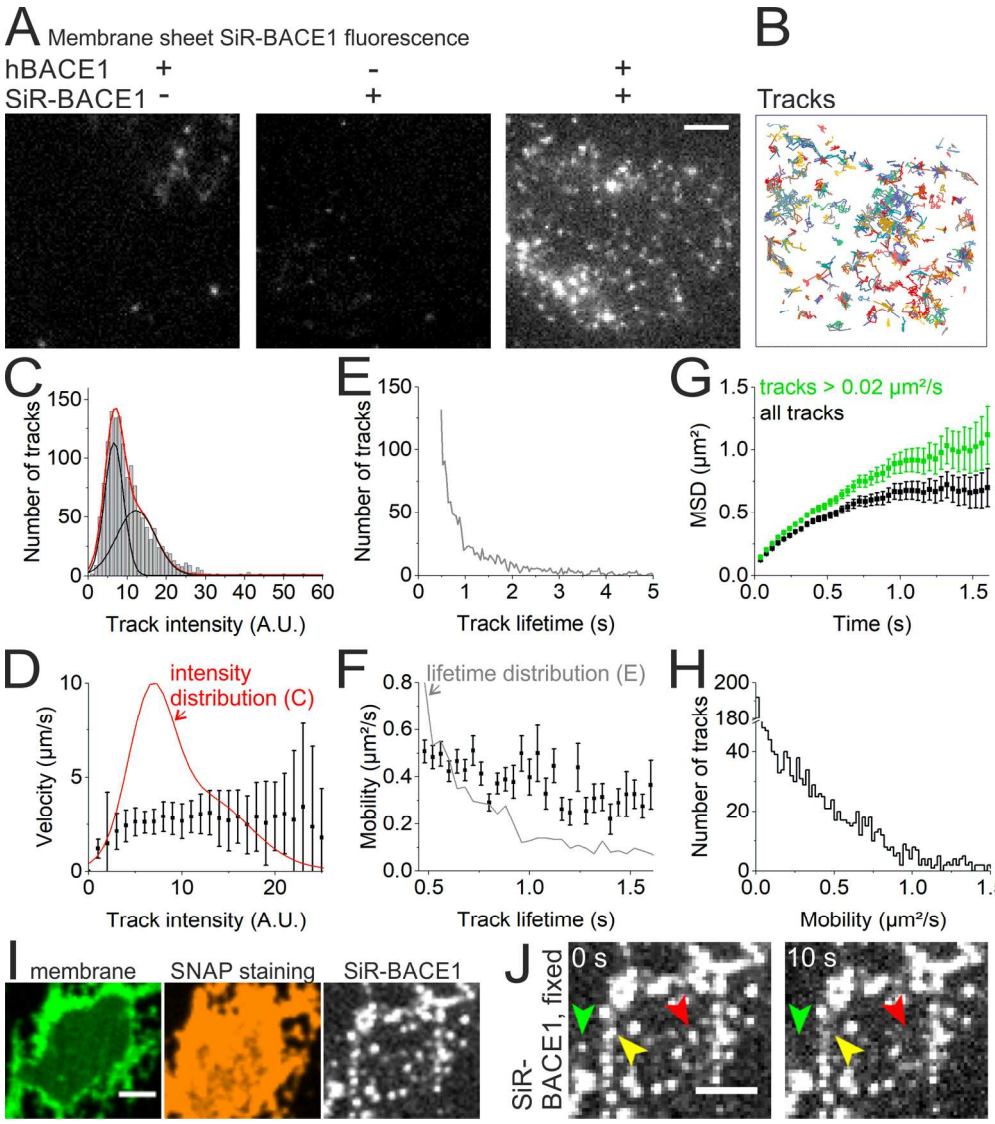

Figure 7

160x177mm (300 x 300 DPI)

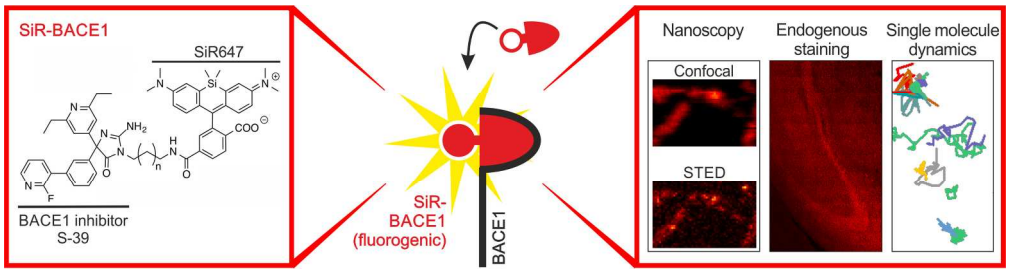

TOC graphic

209x55mm (300 x 300 DPI)